THE VISUALIZATION OF QUANTUM TURBULENCE IN SUPERFLUID ^{4}HE

By

ALEXANDER MARAKOV

A DISSERTATION PRESENTED TO THE GRADUATE SCHOOL
OF THE UNIVERSITY OF FLORIDA IN PARTIAL FULFILLMENT
OF THE REQUIREMENTS FOR THE DEGREE OF
DOCTOR OF PHILOSOPHY

UNIVERSITY OF FLORIDA

2015

To my father

ACKNOWLEDGMENTS

Foremost, I must thank my advisor, Dr. Gary Ihas, for having the faith and courage to allow me to pursue a Ph.D. project far removed from his areas of expertise. Gary has always been ready with advice or an anecdote (often both!) whenever I ran into trouble (not uncommon) with cryogenics or electronics. And, perhaps most importantly, Gary allowed me the freedom to make mistakes, which were often instructive, but then would appear just in time to help me avoid total demoralization and disaster.

The work presented herein was performed at the National High Magnetic Field Laboratory in Tallahassee in collaboration with Jian Gao and under the supervision of Dr. Wei Guo. Thus, my thanks go out to Dr. Steven van Sciver for permitting me to be a member of his lab for the duration of these experiments. Enormous thanks to Dr. Guo not only for his patience, guidance, and advice during these experiments, but also for teaching me almost everything I know about the practical use of lasers and optics in the laboratory during the early days of this experiment. Enormous thanks to my lab mate, Jian Gao, without whom the long nights in lab, seemingly endless equipment repair, and unceasing beam alignment would have been unbearable and impossible. Also thanks to Ernesto Bosque, Joe Hurd, Ram Dhuley and Mark Vanderlaan for their friendship and technical advice during my time at the Cryolab.

The first attempts at performing these experiments occurred in the Reitze lab at the University of Florida. Thus, I must thank Dr. David Reitze for allowing us to use his femtosecond laser. Dr. Vidya Ramanathan deserves my endless gratitude for the extensive advice and assistance she gave to myself, Gary, and Wei when we were coming to grips with the principles of femtosecond laser systems.

Many thanks to Dr. Daniel McKinsey both for his advice during the course of these experiments and for loaning much of the equipment described within. This experiment would truly have been impossible without him.

Thanks to Dr. William 'Joe' Vinen for the many fruitful discussions and experimental suggestions. Consistently, I would find that talking to Joe helped me fit our experiment into the broader context of quantum turbulence work. Additionally, I am grateful for Joe's comments on this dissertation, without which it would be a much poorer document.

Of course, none of this would have been possible without financial support from the University of Florida, the UF Department of Physics and Center for Condensed Matter Sciences, the National Science Foundation (DMR−1007974 and DMR−1007937), Florida State University, the National High Magnetic Field Lab, and the US Department of Energy (DE−FG02_96ER40952). Additionally, I am grateful for funding from the UF College of Liberal Arts and Sciences and the LT24 Graduate Student Travel Fund for supporting travel to International Meetings.

Thanks to Jihee Yang, who on many occasions coated transducers for me and also provided helpful feedback during my practice talks.

Thanks to Bill Malphurs and Mark Link of the UF machine shop, who no doubt have seen enough of me to last a lifetime. Thanks to Pete Axson and Dan Ekdahl of the UF electronics shop and Andy Powell and Eric Stiers of the NHMFL electronics shop without whose considerable efforts I would be buried under a mountain of dead instruments and half-improvised electronic monstrosities. Many thanks to Gregg Labbe of UF Cryogenics services without whom I wouldn't know a helium transfer if it hit me in the face. Gregg also taught me a great deal about vacuum systems, leak checking and cryogenic plumbing. He, along with Jay Horton, assembled the helium infrastructure for our first attempts at the visualization experiment.

Special thanks to my friends, both new ones I've made here in Gainesville and the old ones scattered across the United States. Without you listening to my incessant grumbling about 'lasers' and 'mechanisms', I certainly would have quit a long time ago.

And, of course, I must thank my family, whose support and confidence in me has never wavered. No doubt, they are quite ready for me to end my long exile in Florida!

Especially, I must thank my grandmother, who has doggedly (and sometimes pointedly) kept track of my progress since day one of graduate school. She has experienced more than her fair share of triumph and despair in the laboratory, and has always been ready to lend a sympathetic ear or a word of advice throughout my grad school career.

Lastly I must thank my father, to whom this work is dedicated, though he will never see it. My father taught me the value of patience, kindness, dedication, and a good sense of humor. Without him, I would not be the man I am today.

TABLE OF CONTENTS

LIST OF FIGURES

Abstract of Dissertation Presented to the Graduate School
of the University of Florida in Partial Fulfillment of the
Requirements for the Degree of Doctor of Philosophy

THE VISUALIZATION OF QUANTUM TURBULENCE IN SUPERFLUID ^{4}HE

By

Alexander Marakov

May 2015

Chair: Gary G. Ihas
Major: Physics

Past visualization experiments in superfluid ^{4}He counterflow were severely limited to low heat fluxes to generate reliable data. Ambiguous coupling between micron-sized tracer particles and both components of the superfluid were a consequence of particle size and the scale of investigation. Thus, definite conclusions regarding the behavior of normal fluid flow and normal fluid turbulence could not be made. In light of this, we have developed a novel visualization technique based on the generation of a thin line of He_2 excimer traces via femtosecond-laser field-ionization in order to investigate the motion of the normal fluid component of He-II in counterflow. Studying the drift and distortion of the tracer lines in laminar and turbulent flows, we discover a heretofore unpredicted flow profile in the transition from laminar to turbulent flow. Preliminary evidence is presented to suggest that distorted laminar region is related to the TI/TII transition in superfluid turbulence. Further, velocity PDFs and structure functions are calculated for fully turbulent normal fluid flow. We find no power law tails are present in the velocity PDFs and determine that the turbulent energy spectrum for steady state counterflow is given by $E(k) \propto k^{-2}$ rather than the classical $k^{-5/3}$ power law.

CHAPTER 1
INTRODUCTION

1.1 Turbulence and Liquid Helium

Turbulence, like gravity, is one of the most ubiquitous and relevant physical phenomena that we experience on a daily basis. It manifests constantly during air and sea travel; it is visible in sinks, waterfalls, swimming pools and oceans. Yet turbulence remains one of the last bastions of unsolved physics due entirely to the non-linearity in the Navier-Stokes equations which govern fluid flow,

$$\rho\left(\frac{\partial\vec{u}}{\partial t}+\vec{u}\cdot\nabla\vec{u}\right)=-\nabla p+\mu\nabla^2\vec{u}-\frac{2}{3}\mu\nabla(\nabla\cdot\vec{u})+\rho\vec{g} \tag{1–1}$$

where ρ is fluid density, $\vec{u}$ is velocity, p is pressure, μ is dynamic viscosity and $\vec{g}$ is the acceleration due to gravity (or, more generally, an outside force). The non-linearity of the Navier-Stokes equation comes from the term $\vec{u}\cdot\nabla\vec{u}$. It is this term that is responsible for the transfer of kinetic energy down length scales, also known as the turbulent cascade. Indeed, while turbulence is defined as a chaotic, dissipative phenomenon, the dissipation in classical fluids occurs only at what is called the Kolmogorov length scale, defined as $\eta\sim\epsilon^{-1/4}\nu^{3/4}$ where ϵ is the flux of turbulent kinetic energy per unit mass in k-space and ν is the kinematic viscosity. Above the Kolmogorov scale, in what is called the inertial range, energy is simply transferred from larger length scales to smaller ones. The inertial range is bounded above by the injection scale at which energy is injected into the system. It is also natural to wonder how the energy in the system is distributed across length scales. That is to say, what is the energy spectrum, $E(k)$ of the turbulence? By dimensional analysis, Kolmogorov found that classical turbulence should have energy spectrum $E(k)\propto k^{-5/3}$ where k is the wave vector. Strikingly, every turbulently flowing fluid ever investigated experimentally has exhibited an energy spectrum obeying the power law that Kolmogorov predicted. Thus while exact analytic solutions for motion of turbulent fluid are currently out of the reach of science, we are still able to determine

many characteristics of turbulent flow. One might also consider whether a fluid with very small or even zero viscosity could be turbulent. As it turns out, liquid helium, when cooled below 2.17 K, exhibits superfluidity, which is to say, its flow becomes irrotational.

Although helium was first liquified in 1908 by Kamerlingh Onnes [1], it was not until 1938 that Kapitza, Allen and Misener independently discovered its superfluid properties [2, 3]. The two fluid theory that describes superfluid helium was conceived by Tisza [4] and developed by Landau [5] explicitly to provide a theoretical explanation for the unusual behavior and properties of superfluid helium (frequently referred to as helium II). For the sake of brevity, this document will restrict itself to a brief description of the two fluid theory, second sound, and thermal counterflow. An excellent survey of early experimental results in helium and the development of liquid helium theory can be found in Ref. [6].

In short, the two fluid theory of helium II postulates that the superfluid is actually composed of two, non-interacting, intimately mixed components. These two parts are dubbed the superfluid and the normal fluid with densities ρ_s and ρ_n, respectively. As expected, the densities of the components must sum to the density of the bulk fluid ($\rho_s + \rho_n = \rho$). Additionally, each component has its own velocity field, $\vec{v_s}$ and $\vec{v_n}$. The superfluid component is defined by its irrotationality ($\nabla \times v_s = 0$), and was found to have no viscosity and no entropy, thus it does not carry any heat. Indeed, the aptly named normal fluid is considered to largely act as a classical fluid, as it has all of the entropy of the bulk liquid and also a non-zero viscosity. Strictly speaking, the normal fluid is actually considered to be a gas of elementary excitations (phonons, rotons, maxons) and impurities in the liquid, but this is a conceptual clarification with little bearing on the physics of the two fluid model. Fig. 1-1 shows the superfluid and normal fluid fraction in helium II as a function of temperature [7]. The main body of work described in the following chapters is performed at a temperature of 1.830 K at which $\frac{\rho_s}{\rho_n} = \frac{2}{3}$.

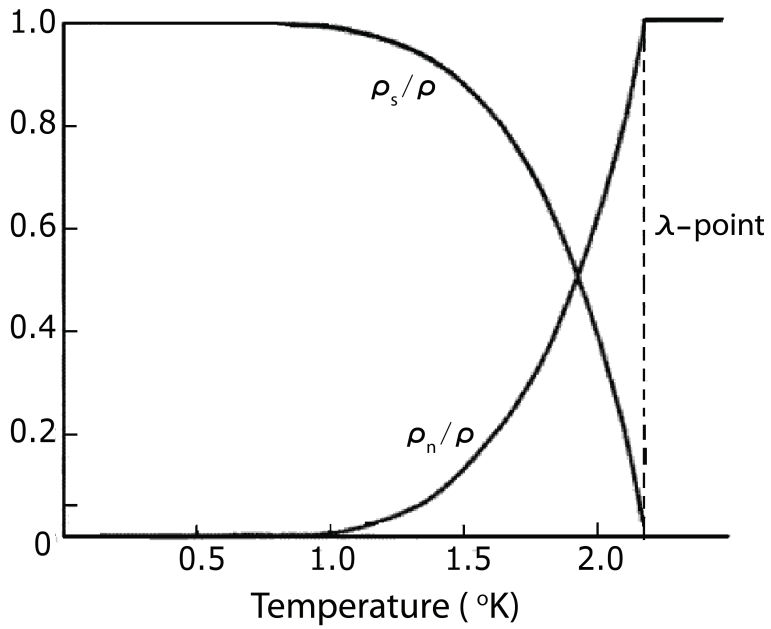

Figure 1-1: The superfluid fraction (ρ_s/ρ) and normal fluid fraction (ρ_n/ρ) as functions of temperature. Above the λ transition, in the helium I state, the entire fluid must be 'normal' (classical). Below the λ transition the superfluid fraction increases rapidly. For temperatures below 1.0 K, the entire liquid is essentially in the superfluid state. [6]

1.1.1 Second Sound

A direct consequence of the two fluid model is the possibility for a second mode of wave propagation. Regular sound, or first sound in helium II, is described as the compression and rarefaction of the entire fluid and so must be a pressure wave. In first sound, both the normal and superfluid components must move together in phase. However, since v_n and v_s are independent velocity fields, there is no *a priori* reason that the fluid components should always move in phase. In situations where the components move opposite each other, or out of phase, there are regions where the local density of normal fluid is higher than super fluid (so temperature is greater than the average temperature of the bulk liquid) and vice versa. This sort of fluid flow configuration results in a wave of temperature or entropy. We call the propagation of a temperature wave second sound (or 2^{nd} sound).

Fortunately, we are not limited to merely qualitative arguments for the existence of 2^{nd} sound. Indeed, starting from the eight hydrodynamic equations for a superfluid, it is possible to derive the existence of two sound modes [6].

$$\rho_s \frac{\partial \vec{v}_s}{\partial t} = -\frac{\rho_s}{\rho}\nabla p + \rho_s S \nabla T \tag{1–2a}$$

$$\rho_n \frac{\partial \vec{v}_n}{\partial t} = -\frac{\rho_n}{\rho}\nabla p - \rho_s S \nabla T \tag{1–2b}$$

$$\frac{\partial \rho}{\partial t} + \nabla \cdot (\rho_s \vec{v}_s + \rho_n \vec{v}_n) = 0 \tag{1–2c}$$

$$\frac{\partial}{\partial t}(\rho S) + \nabla \cdot (\rho S \vec{v}_n) = 0 \tag{1–2d}$$

Here $\vec{v}_{n,s}$, p, $\rho, \rho_{s,n}$ have been defined above and S, T are the entropy and temperature of the fluid, respectively. The hydrodynamic equations listed above are nothing more than the familiar momentum, mass and entropy conservation equations one might encounter in a classical fluid mechanics text, but modified slightly to account for the independent velocity fields, $\vec{v}_s$ and $\vec{v}_n$ and the entropy-less nature of the superfluid component.

We aim to derive two wave modes, one for pressure and one for entropy, so (1–2 a-d) can be manipulated to eliminate v_s and v_n to yield, after dropping second order terms:

$$\frac{\partial^2 \rho}{\partial t^2} = \nabla^2 p \tag{1–3a}$$

$$\frac{\partial^2 S}{\partial t^2} = \frac{\rho_s}{\rho_n} S^2 \nabla^2 T \tag{1–3b}$$

We then use the equations of state:

$$dp = \left(\frac{\partial p}{\partial \rho}\right)_S d\rho + \left(\frac{\partial p}{\partial S}\right)_\rho dS \tag{1–4a}$$

$$dT = \left(\frac{\partial T}{\partial \rho}\right)_S d\rho + \left(\frac{\partial T}{\partial S}\right)_\rho dS \tag{1–4b}$$

in (1–3 a,b) to express T and p as functions of ρ and S in order to obtain the following wave equations

$$\frac{\partial^2 \rho}{\partial t^2} = \left(\frac{\partial p}{\partial \rho}\right)_S \nabla^2 \rho + \left(\frac{\partial p}{\partial S}\right)_\rho \nabla^2 S \tag{1–5a}$$

$$\frac{\partial^2 S}{\partial t^2} = \frac{\rho_s}{\rho_n} S^2 \left[\left(\frac{\partial T}{\partial \rho}\right)_S \nabla^2 \rho + \left(\frac{\partial T}{\partial S}\right)_\rho \nabla^2 S\right] \tag{1–5b}$$

Of course, solving these equations explicitly is not necessary. Instead, we may 'guess' plane wave solutions, (1–6), for ρ and S and check to see if these solutions satisfy (1–5a,b).

$$\rho = \rho_0 + \delta\rho e^{i(kx-\omega t)} \tag{1–6a}$$

$$S = S_0 + \delta S e^{i(kx-\omega t))} \tag{1–6b}$$

We use $\delta\rho$ and δS to denote that the waves are small deviations from the equilibrium state (ρ_0, S_0), else the linearization of (1–2) is invalid. Substituting (1–6) into (1–5) and defining the speed of sound as $u = \frac{\omega}{k}$ we finally conclude that

$$\left[\left(\frac{u}{u_1}\right)^2 - 1\right] \delta\rho + \left(\frac{\partial p}{\partial S}\right)_\rho \left(\frac{\partial \rho}{\partial p}\right)_S \delta S = 0 \tag{1–7a}$$

$$\left(\frac{\partial T}{\partial S}\right)_S \left(\frac{\partial S}{\partial T}\right)_\rho \delta\rho + \left[\left(\frac{u}{u_2}\right)^2 - 1\right] \delta S = 0 \tag{1–7b}$$

where

$$u_1^2 = \left(\frac{\partial p}{\partial \rho}\right)_S \tag{1–7c}$$

$$u_2^2 = \frac{\rho_s}{\rho_n} S^2 \left(\frac{\partial T}{\partial S}\right)_\rho \tag{1–7d}$$

If we let $u = u_1$, then to satisfy (1–7a,b) δS must vanish. Thus when there are density oscillations, entropy remains constant and we find that we have described first sound.

Conversely, if $u = u_2$, then density must remain constant while entropy (or temperature) oscillates in the fluid which is consistent with the qualitative description of 2^{nd} sound given above. The speed of 2^{nd} sound is presented in Fig. 1-2. It is found to vary slowly near 20 m/s from 1.0 K to roughly 1.8 K, after which it grows slightly and plummets to 0 m/s at the λ-point [8].

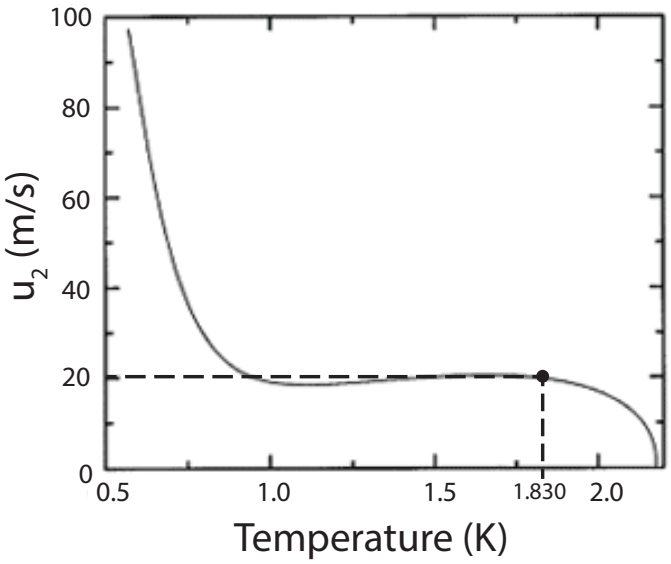

Figure 1-2: The velocity of 2^{nd} sound, u_2, as a function of temperature up to the lambda point. The dashed lines indicate the 2^{nd} sound velocity for the experiments conducted in the following chapters. [9]

1.1.2 Quantum Turbulence

Central to the two fluid theory is the requirement that the superfluid be irrotational [5]. That is to say, $\nabla \times \vec{v}_s = 0$. However, the nature of turbulence requires that there be some sort of rotation present. This paradox is resolved by the introduction of line defects into the superfluid. These defects change the geometry of the bulk fluid from a simply connected region to a multiply connected region. In a multiply connected geometry, the condition $\nabla \times \vec{v}_s = 0$ is satisfied, but the circulation equation (1–8) can still yield a non-zero result. Indeed, because $v_s = \nabla S$, where S is the phase of the macroscopic wave function of the Bose-Einstein condensate of the superfluid, we find that the circulation is actually quantized [10]:

$$\oint \vec{v}_s \cdot d\ell = nh/m \tag{1–8}$$

The integration is performed along a path around a line defect, n is an integer winding number, h is Plank's constant and m is the mass of a helium atom. In superfluid helium, n is restricted to be 1, so we define the quantum of circulation $\kappa \equiv h/m$. We then rename the line defect to be a quantized vortex line, or if the line terminates upon itself, it is termed a quantized vortex ring. In principle, quantized vortex lines can be nucleated only above some critical flow velocity, which should not be confused with the Landau critical velocity of 60 m/s at which elementary excitations are created in the fluid [5]. In practice, the critical velocity for vortex line creation is found to be several orders of magnitude below the Landau critical velocity (see [11–14] for relevant experiments on critical velocities). At flow velocities above the empirical critical velocity, a vortex line tangle is said to form. *It is this tangle and its interactions with the normal fluid through mutual friction that is defined to be quantum turbulence.* The vortex line tangle possesses all of the expected properties of turbulence: it is chaotic, it has some sort of rotation, it is diffusive, and it is dissipative. The mutual friction force between the normal and superfluid components is the source of dissipation and, because of the finite relative velocity between the fluids in counterflow, this dissipation is expected to occur at *many* length scales, possibly all the way up to the injective scale itself. What then, can be said about the energy spectrum of this kind of quantum turbulence? Recently, this has become an experimentally tractable question. The remainder of this dissertation is devoted to describing the experiment built to empirically characterize the quantum turbulence of counterflowing superfluid ^{4}He.

1.1.3 Thermal Counterflow

In superfluid helium, heat is carried entirely by the normal fluid and mass conservation requires that the superfluid component flow opposite to the normal fluid. Thus, application of any heat flux to a volume of helium II will cause counterflow. Thermal

counterflow turbulence has no known classical analogues, and there exist a variety of effective techniques to probe vortex line density in the fluid. The counterflow velocity is only a function of applied heat heat flux, q, density of the liquid, ρ, entropy per unit mass, s, and the temperature of the bath, T, and is expressed in the following way:

$$v_n = \frac{q}{\rho s T} \tag{1–9}$$

The first, thorough series of studies of counterflow turbulence were performed and published by Vinen [11, 15–17]. Energy dissipation in counterflow turbulence occurs largely in the interactions between the vortex line tangle and the normal fluid. This interaction is called the mutual friction [18]. These experiments were the first to show that the mutual friction between the normal fluid and quantized vortex lines was proportional only to the relative velocity between the fluid components $(v_s - v_n)$. Vinen's experiments performed with steady-state counterflow determine an equation for 2^{nd} sound attenuation as a function of heat flux:

$$\alpha' = C(W - W_0)^2 \tag{1–10}$$

where α' is the attenuation, C is a constant of proportionality, and W, W_0 are applied and critical heat fluxes, respectively. The equation for line density, L, as a function of attenuation is

$$L = \frac{6\pi\Delta}{\kappa B}\left(\frac{A_0}{A} - 1\right) \tag{1–11}$$

where Δ is resonance peak width, κ is the constant of circulation, B is the mutual friction constant and A_0 and A are the initial resonance peak amplitude and attenuated amplitude, respectively. In (1–11), $\left(\frac{A_0}{A} - 1\right) = \alpha'$. Combining (1–10) and (1–11), expressing heat flux in terms of counterflow velocity V and taking the square root we

are able to produce an equation for the average spacing between vortex lines, ℓ (where $\ell = L^{1/2}$) [19],

$$\ell = \gamma(V - V_0) \tag{1–12}$$

where V is counterflow velocity, V_0 is the critical velocity and γ is the collection of relevant constants. Practically, γ is used as a fit parameter for comparison between different steady-state counterflow experiments. In terms of experimental considerations, the best sensitivity is achieved by resonances with small full-width half-max (FWHM) value and large amplitude.

Experiments in very small ($\mu m - mm$) channels served not only to further confirm Vinen's initial work, but also to unearth another feature of superfluid turbulence: the TI/TII transition. The first evidence, largely overlooked, of the existence of a less turbulent counterflow regime, later dubbed the TI state, appears in Fig. 3 of Ref. [11]. Subsequent experiments [12–14, 20, 21] explored and characterized the transition from TI turbulence to the more familiar TII turbulence described by (1–12). In small channels of low-aspect ratio (square or circular cross-section) the TI/TII states are found to be reproducible with consistent critical velocities as a function of size. Further, it was found that the features of the TI and TII superfluid turbulence states are independent of characteristic tube size for circular tubes. It would not be unreasonable to expect the same to be true in channels with square cross-section, but currently no experimental evidence exists to support such an expectation.

It is noteworthy that there exists a significant body of work relating to the decay of transient counterflow turbulence. The decay of counterflow turbulence in a wide (9 mm) channel (at 1.6 K) exhibits a number of interesting features [22]. First, it is clear that the vorticity in the channel does not always decrease monotonically after heat flux is switched off (though this was seen in earlier work). Indeed, the vorticity is observed to either flatten out for some time (up to several seconds!) or even increase, forming a 'bump' in the decay

plot. Secondly, for each probed heat flux, the vorticity decay eventually assumes a classical form. That is to say, the vorticity decay obeys a $t^{-3/2}$ power law in the later stages of decay.

In both the steady state and transient counterflow cases, plenty of data exist describing the behavior of the vortex line tangle and superfluid component. However, many serious questions remain, not least of which is the question of the normal fluid flow. In the transitions to turbulence, does normal fluid flow instability cause turbulence in the superfluid? Is normal fluid turbulence totally independent of the superfluid flow? When does the normal fluid become turbulent? How does the decay of normal fluid turbulence compare to decay of superfluid vorticity in the channel? All of these questions must be answered to move toward a complete description of quantum turbulence. The way forward absolutely requires development of effective visualization techniques in superfluid helium, the subject of this dissertation.

1.2 Visualization

Although quantum turbulence in superfluid ^{4}He has been a subject of study for well over half a century, flow visualization, one of the most powerful and common experimental techniques in classical turbulence, has only recently been implemented in helium-II. The best known such experiments were Particle Image Velocimetry and Particle Tracking Velocimetry (PIV/PTV). The basic experimental scheme requires that helium-II be seeded with small ($\sim \mu$m) spherical particles of polystyrene [23] or hydrogen 'snowballs' [24, 25]. Particle positions are detected by shining a laser sheet through the experimental volume and capturing light reflected from the tracer particles with a CCD camera. PIV/PTV experiments did yield some interesting data about superfluid helium. Zhang and Van Sciver discovered vortices upstream of a fixed cylinder in turbulent counterflowing helium II [26]. The first visualizations of quantized vortex lines were achieved by Packard et al. in rotating cryostats in which both single vortices and arrays of vortices were observed [27, 28]. An experiment by Bewley seems to show decorated quantized vortex lines with

hydrogen snowballs, possibly providing the first images of quantized vortices in counter flowing superfluid helium [24], but no quantitative proof is given. Similar subsequent experiments by Paoletti et al. show particle velocity statistics that are, in some cases, consistent with the expected velocity of the vortex line tangle in thermal counterflow [29] Unfortunately, particle velocimetry techniques suffer from ambiguity at high heat flux (high counterflow velocity) due to the interactions between particles and quantized vortices [29, 30]. PIV experiments showed that, in thermal counterflow, the tracer velocity does not match that of the normal fluid, as was originally expected [31]. Subsequent PTV experiments demonstrated that the tracers undergo sudden changes of direction, which were interpreted to correspond to the tracers either binding to or being dislodged from the quantized vortex lines [25]. While such experiments have yielded a wealth of information about the interaction of tracer particles with vortex lines [32, 33], and, at low heat flux, demonstrated the existence of two velocity fields (v_n&v_s), comparatively little was learned about the flow profiles of the normal fluid and superfluid components at high heat fluxes. Some visualization work has been done using neutron tomography of ^{3}He seeded helium-II. By using atoms of ^{3}He as tracers, this technique side-steps some of the serious issues inherent in the PIV/PTV experiments. Namely, above 1 K, the ^{3}He molecules essentially act as normal fluid, so there is no ambiguous coupling between tracer and the superfluid/normal fluid components. Additionally, ^{3}He does not spontaneously aggregate or adsorb onto cell walls, unlike the impurities used as tracers in other experiments. The only such experiment was limited in its spacial resolution by the comparatively large size of the neutron beam ($\sim$ 4 mm FWHM) and in its time resolution by the need to raster the beam in order to develop a full picture of the experimental volume [34]. Naturally, this puts strong restrictions on the range of heat fluxes that can be investigated in such a setup. In principle, neutron-tomography experiments of this sort can be improved by refining the experimental design, but it is likely that such a visualization scheme will remain most suitable for steady-state flow mapping rather than the study of dynamical

processes. Given the difficulties encountered in superfluid flow visualization thus far, it is natural to ask for a tracer that unambiguously couples to the normal fluid at T > 1 K, does not contaminate the superfluid, has a reasonably long lifetime and does not require extremely specialized facilities such as beam lines at national laboratories. One such candidate tracer exists: the excited helium dimer.

1.2.1 Helium Excimers

The excited helium dimer, more commonly called the helium excimer (He_2^*), has a number of agreeable qualities that make it an ideal tracer in helium. While the spin-singlet state of He_2^* has a radiative lifetime measured in nanoseconds, the spin-triplet state has a much longer lifetime ($\sim$ 13 s in vacuum [35]) due to a forbidden spin-flip. Additionally, in cold dense gas or liquid, He_2^* molecules form small bubbles, with radius about 7 Å [36], in the $a(0)$ state and 12 Å in the $d(0)$ state, which gives them an exceedingly short viscous relaxation time. The viscous relaxation time, τ, is a measure of how quickly the particle's motion relaxes to that of the fluid in which it is located and is given by [33]

$$\tau = \frac{2\rho_\circ a_p^2}{9\mu_n}, \qquad \rho_\circ = \rho_p + \frac{\rho}{2} \tag{1–13}$$

where ρ_p is the density of the tracer particle, ρ is the density of the fluid, a_p is the radius of the particle, and μ_n is the viscosity of the normal fluid. For superfluid helium at 1.830 K and excimers with bubble radius 7 Å, the viscous relaxation is only 4.4 ps. Thus, the velocity of excimers which interact with vortex lines relaxes to that of the normal fluid in an extremely short time. In light of this, it is quite reasonable to expect that, on the probing scale of our experiments, helium excimers are entirely entrained by the normal fluid at temperatures above 1 K. The visualization of these tracers is performed entirely by laser-induced fluorescence (LIF). Experiments by Benderskii et al. in both liquid and cold, gaseous helium indicated that the helium excimer can be made to fluoresce at several different wavelengths, the most dominant of which was 640 nm. A complete characterization of laser-induced fluorescence of He_2^* in superfluid helium can be found in

Wade Rellergert's dissertation [37]. What follows will be a brief summary of the relevant characteristics and requirements of LIF experiments in superfluid helium. Fig 1-3 shows a schematic drawing of the energy levels of He_2^* in helium-II.

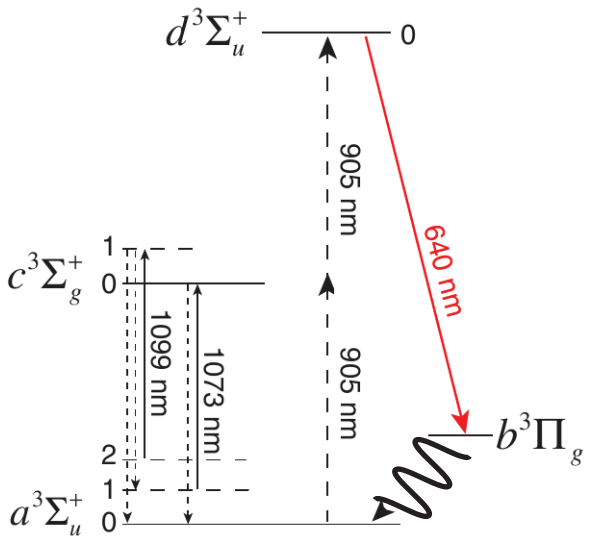

Figure 1-3: Energy levels of He_2^* in liquid helium. The $a^3\Sigma_u^+ \rightarrow c^3\Sigma_g^+ \rightarrow d^3\Sigma_u^+$ transition is pumped by two 905 nm photons. 640 nm fluorescence from the $d^3\Sigma_u^+ \rightarrow b^3\Pi_g$ transition will be collected by an ICCD camera. Excimers trapped in the long-lived $a(1)$ and $a(2)$ vibrational states are repumped by cw fiber lasers with wavelengths 1073 nm and 1099 nm, respectively.

In cold helium gas, the energy states are such that the $a^3\Sigma_u^+ \rightarrow c^3\Sigma_g^+$ requires a 919 nm photon and $c^3\Sigma_g^+ \rightarrow d^3\Sigma_u^+$ requires a 1047 nm photon. Conveniently, in bulk liquid, the excitation scheme for excimers in bulk superfluid exploits the broadening[36] of the $c^3\Sigma_g^+ \rightarrow d^3\Sigma_u^+$ transition such that the $a^3\Sigma_u^+ \rightarrow c^3\Sigma_g^+$ and $c^3\Sigma_g^+ \rightarrow d^3\Sigma_u^+$ transitions can each be excited with a 905 nm photon. About 90% of excimers in the $b^3\Pi_g$ quench to the $a(0)$ state. Thus, 10% of the excimers end up trapped in either the $a(1)$ or $a(2)$ long lived ($\tau \geq 100$ ms) vibrational states. Without cycling the trapped excimers, the fluorescence intensity from the $d^3\Sigma_u^+ \rightarrow b^3\Pi_g$ transition quickly drops to a steady state value of $\sim 25\%$ of the initial intensity. However, when continuous wave (cw) repumping laser beams with wavelengths 1073 and 1099 nm are introduced, the steady state fluorescence intensity has

been shown to be $\sim 85\%$ of the initial value [37]. Crucially, two-photon excitation allows for a large separation between excitation and fluorescent wavelengths, so the former can be filtered out from the detector.

1.2.2 Penning Ionization

Previous experiments have used radioactive sources [37] and high electric fields at the tips of sharp tungsten needles [38] to generate large clouds of excimers. Further work demonstrated that the excimers follow the normal fluid [38] and produced evidence of turbulence at high heat flux [39]. However, due to low excimer density, the images captured in those experiments were averages of 40 exposures, thereby averaging out important details of the turbulent flow. To study the finer features of superfluid turbulence, it is important to obtain an excimer density such that the emitted fluorescence is sufficient to allow for high quality single-shot images. One such method is excimer creation by laser-field ionization [40]. The beam waist and laser power can be controlled to create long, thin lines of excimers with high densities (up to 10^{13} cm$^{-}3$ [41]). However, it is important to consider the mechanisms by which excimers might be eliminated from the ionization volume, thereby limiting the density of excimers in a finite volume. The dominant mechanism for excimer removal is due to collisions between pairs of molecules. This process is commonly referred to as Penning ionization or bimolecular decay. In general, Penning ionization occurs when an excited metastable molecule M^* collides with some other molecule or atom A, which results in de-excitation of M^* and the ionization of A [42]:

$$M^* + A \rightarrow M + A^+ + e^-$$

Keto et al. [43] performed an experimental investigation of the Penning ionization of metastable ($a^3\Sigma_u^+$) helium excimers. The Penning ionization between two He_2^* molecules can be described as [41]

$$He_2^* + He_2^* \rightarrow He_2^{**} + 2He \tag{1–14}$$

where He_2^{**} can be said to be a more highly excited state than He_2^*. Further, they determine that, for helium excimers in the $a^3\Sigma_u^+$ state near 1.830 K, the decay constant for Penning ionization of He_2^* is $\alpha \sim 4 \cdot 10^{-10}$ cm^3/s. The corresponding equation for excimer density (in the absence of a source term) is [43]

$$n(t) = \frac{n_0}{1 + \alpha n_0 t} \tag{1–15}$$

where $n(t)$ is the excimer density, n_0 is the initial excimer density, α is the Penning ionization decay constant and t is decay time. Thus it is clear that, if the rate of excimer creation is known, the steady state concentration of excimers can be determined as a function of laser repetition rate (rep-rate) and laser power per pulse. Specifically, if the number of excimers is increased by a factor of 2^m per pulse (where m depends on laser power per pulse, described for this experiment at the end of § 2.1), then, in the steady state, the excimer density must decay by a factor of 2^m between pulses. It then follows that the steady state excimer density, n_{ss}, in a train of laser pulses is

$$n_{ss} = \frac{2^m - 1}{\alpha t_{rep}} \tag{1–16}$$

where t_{rep} is the time between laser pulses. Since the intensity of fluorescence will be directly proportional to excimer density in the illuminated volume, the Penning ionization will have a significant impact on the image quality and observation time scales in the experiment described in Ch. 2.

CHAPTER 2
EXPERIMENT AND PROTOCOL

This chapter presents the details of an experimental apparatus designed to perform LIF experiments in superfluid ^{4}He. § 2.1 describes the components of the apparatus and their configurations relative to each other. Most of the components are commercially available, with the experimental channel being custom made. Additionally, § 2.1 includes the details of the laser beam profile characterization and its manipulation by the relevant optics to achieve the necessary energy fluxes required to produce a thin He_2^*. § 2.2.3 presents the details of the 2^{nd} sound apparatus for probing vortex line density, including the design of the oscillating superleak transducers, electronics setup and considerations related to resonance peak selection. § 2.2.1 primarily concerns preliminary experiments performed to characterize the actual performance of the femtosecond laser in helium as a function of helium density. We find that thin excimer lines can be created in helium gas near standard temperature and pressure (STP, T = 273 K and P = 100 kPa) through multi-photon ionization and that a longer line can be created in the superfluid just below the breakdown threshold. Finally, § 2.2.2 shows evidence that there is no excess laser heating in the superfluid since there is no deformation of the excimer line under zero heat flux conditions at long drift times.

2.1 Experiment Design

A schematic of the experimental channel is shown in Fig. 2-1. We mount a stainless steel channel of square cross-section with inner side length 9.4 mm and total length $\sim$ 300 mm at the bottom of a temperature controlled, bath-pumped helium cryostat (custom design, manufactured by American Magnetics). Most of the steel channel components were machined at the National High Magnetic Field Laboratory in Tallahassee, FL, while the 2^{nd} sound cube and transducers were machined at the University of Florida, and the thin, sapphire windows were purchased from Thorlabs. At the bottom of the channel, we place a planar heater (essentially a thin-film resistor, 404 Ω) to drive thermal counterflow. The

channel runs through a stainless steel cube equipped with three thin, sapphire windows, two of which are mounted on arms, removing them from the focused beams to avoid the possibility of laser damage. The lower inset in Fig. 2-1 shows a side-section view of the visualization cube. It is important to note the thin slits ($\sim$ 4 mm) cut into the channel rather than the windows one would expect at this position. Again, this is to avoid laser damage due to the focusing of the fs beam at this point. Although the energy fluence of the femtosecond laser beam for experiments on liquid helium proves to be below the damage threshold of sapphire (between $5 - 11$ J/cm^2) [44], experiments on gaseous helium at high temperatures, such as those shown in Section 2.2.1, can brush the damage fluence threshold, causing sparking and burns on the window. While windows damaged in this way are unlikely to shatter, the damaged areas do tend to significantly distort the beam profile of any laser beams incident on the spot. A distorted beam profile, especially that of the fs laser, leads to unpredictable excimer generation and ionization of the liquid helium. Just below the visualization cube is the so-called "2^{nd} sound cube", on which can be mounted two oscillating superleak transducers. One transducer will generate 2^{nd} sound resonances and the other will act as a detector. The averaged vortex line density in the liquid can be calculated from the attenuation of the resonance amplitude (§ 1.1.3). See section 2.2.3 for a more detailed description of the 2^{nd} sound experimental technique. Finally, the temperature of the liquid helium in the experiment is determined by the saturated vapor pressure curve of helium. A pressure transducer controlling an electronic valve keeps the temperature of the bath constant to within 1 mK. The thermometer is a four wire cernox resistor, placed at the top of the channel, which is calibrated from 300 K to 4.2 K and from 2.17 K to nearly 1.5 K.

The femtosecond laser system (Spectra Physics) consists of a Mai Tai femtosecond laser source, which is fed into a Spitfire Ace regenerative amplifier (pumped by an Empower 20 W green laser). The output from the Spitfire Ace is a stable, nearly Gaussian ($M^2 = 1.04$; M^2 values close to 1 indicate that the beam profile is very close

to Gaussian [45]) beam with pulse length 35 fs and an initial maximum repetition rate 1 kHz. Most of the experiments performed in section 2.2.1 use a rep-rate of 1 kHz. However, the results detailed in chapter 4 are obtained with the Spitfire Ace upgraded to operate at a maximum rep-rate of 5 kHz.

The imaging laser is an EKSPLA Nd:YAG laser with fixed wavelength of 905 nm, which can be operated at either 1 kHz or 500 Hz. We chose 500 Hz. The imaging beam is focused by two cylindrical lenses to have a roughly rectangular shape with width 1.5 mm and height 4 mm. In order to saturate the $a^3\Sigma_u^+ \rightarrow d^3\Sigma_u^+$ transition in the illuminated volume, the imaging laser must deliver 2.5 mJ/cm^2 per pulse [37]. Two fiber diode continuous wave (cw) lasers are required to liberate excimers trapped in the $a(1)$ and $a(2)$ vibrational states. They operate with wavelengths 1073 nm and 1099 nm, respectively, and are aligned onto the imaging laser before passing through the same cylindrical lenses. After focusing, the width of the cw lasers is comparable to that of the imaging beam, but, due to the large initial beam size, the focused height is considerably greater. Both cw lasers deliver approximately 13 W/cm^2 at the focal plane, some of which is intercepted by either the channel body or the thermal shielding. To minimize the heat load from the cw lasers, we ensure that they are only on for a short time: 17 ms at most. The effect, or lack thereof, of this on excimer line quality is discussed in section 2.2.2.

A custom made intensified charge-coupled device (ICCD) camera (PI-MAX II from Princeton Instruments) is placed facing the front of the visualization cube. Although the 640 nm emission peak of He_2^* is dominant, the light from the excimer line is still expected to be quite dim. Thus, most of the modifications to the camera are centered around lens coatings and hardware upgrades that improve the quantum efficiency of the detector for the relevant wavelength. A lens with focal length 15 cm is installed on the cryostat's nitrogen shield to ensure that the channel takes up the majority of the camera's field of view. As mentioned in § 1.2.1, that the fluorescence wavelength we are detecting is significantly smaller than the imaging and cw laser wavelengths is an advantageous

consequence of the LIF scheme we are using (see Fig. 1-3). We filter out unwanted light by installing a 640 nm bandpass filter with a full-width half-max (FWHM) bandwidth of 20 nm on the camera without worrying about additional light being created by higher energy photons from the excitation lasers.

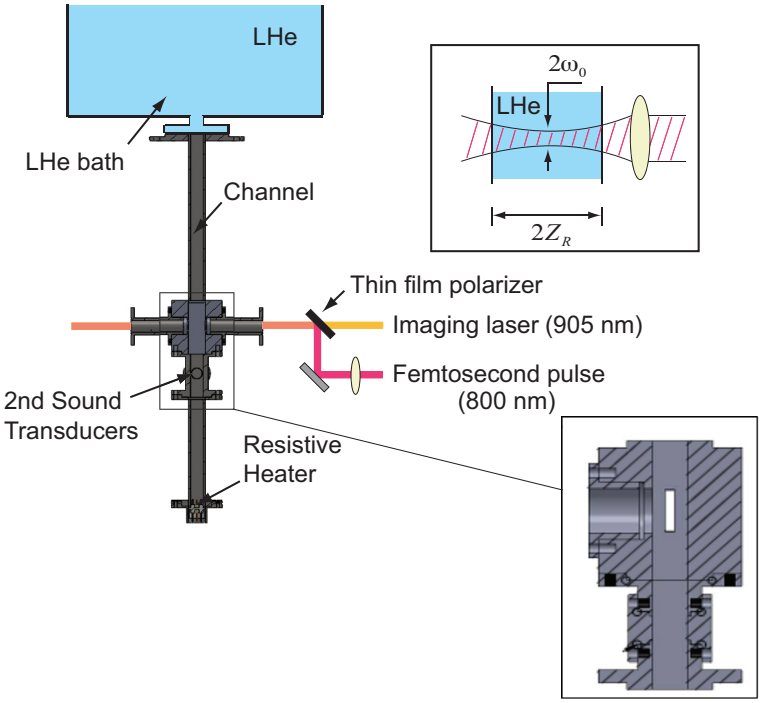

Figure 2-1: A schematic diagram of the stainless steel experimental channel. The channel has square cross-section with side length 9.4 mm and total length $\sim$ 30 cm. It is bolted to a bath-pumped cryostat and therefore shares its liquid with that of the cryostat itself. A thermometer is placed near the top of the channel and is used in conjunction with an electronic valve to regulate the temperature of the bath. The 'visualization cube' has two protruding arms sealed with thin sapphire windows. The fs and imaging beams are aligned to be collinear on the center of the visualization cube arms so that the beams can pass unobstructed through the experimental volume. The ICCD camera is placed facing the third window in the visualization cube (facing into the page). Just below the visualization cube is the 2^{nd} sound cube on which are mounted two oscillating superleak transducers, which generate and detect 2^{nd} sound waves. The attenuation of these waves probes the average vortex line density in the experimental volume. The resistive heater (404 Ω) at the bottom of the flow channel generates thermal counterflow. The inset shows a sketch of the fs laser beam profile ($1/e^2$ width) as it passes through the experimental volume.

The upper inset in Fig. 2-1 shows a sketch of the fs beam profile as it passes through the channel. Naturally, the focusing lens is placed such that the beam waist is in the

center of the channel. Since it is possible for the channel to shift during cool-down, the fs beam focusing lens is mounted on an optical rail so that the beam waist can always be placed mid-channel. Additionally, we chose the focal length to give a Rayleigh range half the length of the channel. For a Gaussian beam, the $1/e^2$ beam width, ω (this is $\frac{\sqrt{2}}{\sqrt{ln(2)}}$FWHM), as a function of distance from the focal plane, z, is given by

$$\omega(z) = \omega_0 \sqrt{1 + \left(\frac{z\lambda}{\pi\omega_0^2}\right)^2} \tag{2–1}$$

where ω_0 is the diameter of the beam waist and λ is the wavelength of light. The Rayleigh range, which is the distance from the focal plane at which the cross-sectional area of the beam doubles, is defined to be $z_R = \frac{\pi\omega_0^2}{\lambda}$. Given this convenient definition, we have a way of choosing the optics and laser power such that there is sufficient energy flux (found to be $I = 5 \cdot 10^{13}$ W/cm^2 at the focal plane [41]) throughout the width of the channel to create a thin line of excimer molecules. Indeed, not only must the energy flux be sufficient, but also it must not, at any point, exceed the ionization breakdown threshold of liquid helium (discussed in section 2.2.1). Fig. 2-3 shows the measured fs beam profile and $1/e^2$ width of the beam profile as a function of distance from the focal plane. The data show that, when passed through a lens with focal length 75 cm, the beam profile is a nearly perfect Gaussian with $M^2 = 1.04$ and Rayleigh range 5.5 mm.

Further, passage of the beams through the experiment is controlled by two shutters. The first, an electro-mechanical solenoid shutter (Newport, model 76993 Electronic Fast Shutter), is paired with the fs laser. It has minimum open time of about 8 ms with a characteristic open/closing time of $\sim$ 4 ms. At a rep-rate of 1 kHz or below, this provides reasonably good control of the fs laser pulses passing through the channel. At much higher rep-rates, such as 5 kHz, the shutter is unable to provide anything better than coarse control of the fs laser. In principle, with two such shutters, it is possible to select exactly how many laser pulses will be passed through the channel, even at 5 kHz. Above a certain number of fs laser pulses, the intensity of the excimer line fluorescence is capped by the

steady state excimer density, so such rigorous control is not necessary. In light of this, we chose a one shutter system for both the fs and imaging lasers in order to simplify the experiment as much as possible. For control of the imaging and fiber lasers we use a slower, mechanical shutter (Thorlabs, SH05 optical beam shutter) with minimum open time 17 ms and characteristic open/close time of ~ 8 ms. As indicated above, the imaging laser is operated at a rep-rate of 500 Hz, so even such a slow shutter can provide adequate control of the 905 nm pulses. Fig. 2-2 provides a schematic representation of the optical bench layout with all relevant optical components.

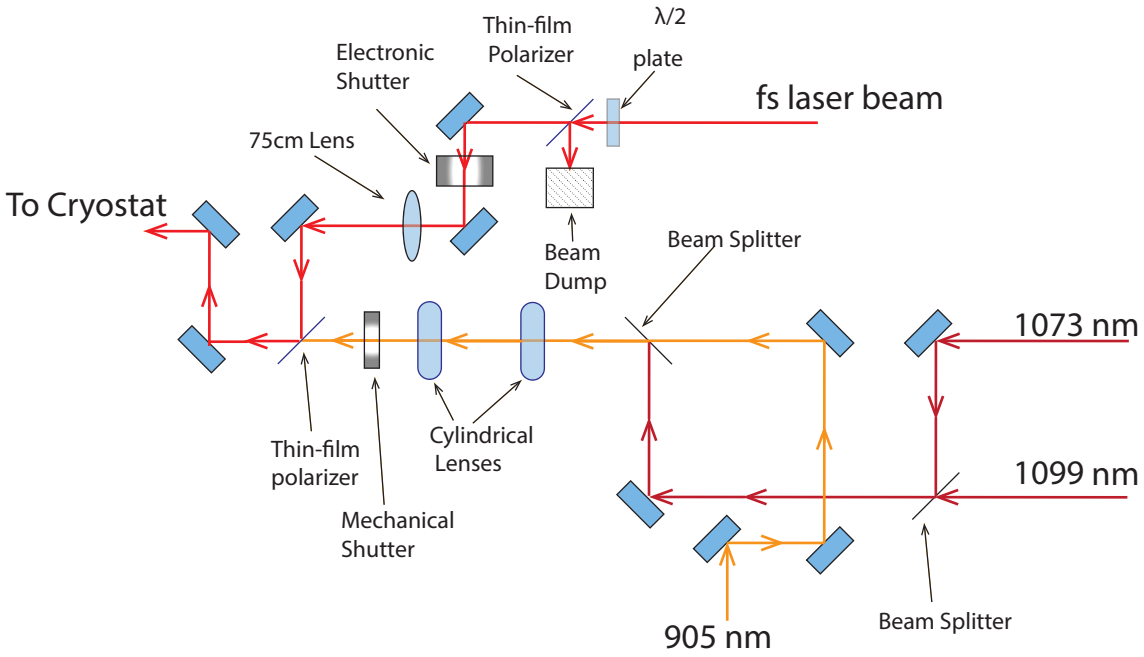

Figure 2-2: A schematic drawing of the optical bench for this experiment. The imaging lasers (905 nm, 1073 nm and 1099 nm) are aligned onto each other using beam splitters and then passed through two cylindrical lenses to obtain the necessary profile. Most critically, the 905 nm laser must be focused so that it is $\sim$ 1 mm wide and $\sim$ 4 mm tall so that it may pass through the slits in the channel walls and also pump the excimer line when it moves during experiments. The SH05 mechanical shutter controls the entry of the imaging lasers into the channel. The femtosecond laser power is controlled by half-wave plate (λ /2 plate) and a thin film polarizer. The Spitfire Ace always outputs 4W of laser power, the vast majority of which is sent into the beam dump. The remainder of the fs laser power is then sent through the fast Newport 76993 shutter, through the 75 cm focusing lens and aligned with the imaging beams with another thin-film polarizer. The final two mirrors allow the collinear beams to be carefully aligned through the slits in the channel.

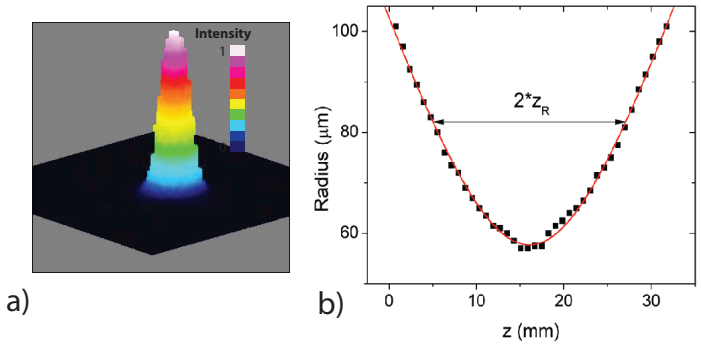

Figure 2-3: (a) Measured cross-section intensity of the femtosecond laser beam at the focal plane. The profile is a nearly perfect Gaussian beam with $M^2 = 1.04$. b) The measured $1/e^2$ width of the femtosecond laser beam as a function of position z along the direction of propagation. The data are fit to Eq. 2–1 (red line), which gives a Rayleigh Range of 5.5 mm. The error bars are smaller than the data points.

The experimental timing is shown in Fig. 2-4. The heater is activated at the specified power for at least 15 s prior to opening the fs laser shutter to ensure that thermal counterflow has fully developed before data collection. Subsequently, the fs shutter is opened, usually for the minimum possible time at 5 kHz since even as few as 10 pulses are expected to be sufficient to reach a steady-state density of helium excimers. After excimer line creation we wait some time denoted as t_{drift} to allow the excimers to be carried with the normal fluid. For experiments at low heat flux, t_{drift} can be as large as 900 ms (at which point image averaging is required). However, in order to extract the structure function from single-shot images, t_{drift} mustn't exceed the eddy turnover time, since the turnover time gives the maximum lifetime of the eddy. For flows with eddy size R and velocity increment $\delta u(R)$ across the eddy, the eddy turnover time,τ, is given by $\tau = \frac{R}{\sqrt{\langle \delta u(r)^2 \rangle}}$ [46]. From our empirical velocity fluctuation data, flow driven by a heat flux of 300 mW/cm^2 has turnover time of about 51 ms at the smallest scales (200μm). While for 225 mW/cm^2 the turnover time increases to about 100 ms at the same scale. In practice, t_{drift} must be chosen to be large enough so that distortions of the excimer line can be resolved, but less than the eddy turnover time so that eddy properties can still be probed.

After the drift time has elapsed, we open the imaging shutter to pass through both the 905 nm pump pulses and the 1073 and 1099 nm CW fiber laser beams for vibrational level cycling. Empirically, we find that image quality does not noticeably improve when averaging more than 6 imaging pulses. The ICCD camera micro-channel plates (MCP) are set to trigger for each 905 nm pulse, thereby collecting *only* fluorescence light and minimizing pollution of the signal by outside light sources. A set of six imaging pulses is collected by the camera and then the registers are shifted and read, defining that set of six as a single shot. At the maximum achievable counterflow velocities, $\sim$ 2 cm/s, the movement of the normal fluid between imaging pulses is on the order of 40 μm, significantly smaller than the width of the excimer line at its narrowest point. Therefore, smearing of the image due to movement between MCP triggers is not expected to be a measurable effect.

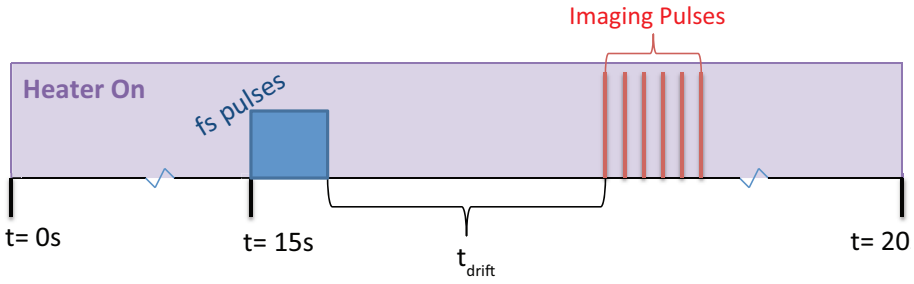

Figure 2-4: Schematic diagram of experiment timing for all steady state counterflow visualization experiments. Initially, the resistive heater at the bottom of the experimental channel is turned on for at least 15 s to ensure fully formed counterflow. The fs laser is then allowed to pass through the channel to create the maximum achievable density of excimers. Some time t_{drift} is allowed to elapse between excimer creation and imaging pulses. Six imaging pulses are found to create the best fluorescence signal. More pulses do not produce a noticeable improvement in image quality. t_{drift} can range between $25 - 900$ ms depending on the magnitude of the heat flux.

The nature of the excimer creation mechanism, controlled electron avalanche ionization (see 2.2), necessarily puts an upper bound on the heat fluxes at which quality fluorescence images can be captured. Benderskii et al. determined that each fs laser pulse multiplies the number of excimers in a given volume of LHe by a factor of 2^m.

They show that the exponent m is determined by the ratio of incident energy per pulse of the laser to the energy per pulse required to double the number of ions. That is to say, $m = W/W_2$ where $W_2 = 13\mu$J/pulse [41]. We find that at 60μJ/pulse we are just under the breakdown threshold of liquid helium at T = 1.830 K (see § 2.2.1). Based on these values, $m = 4.62$ in our case. Between pulses, the excimers undergo Penning ionization decay (see § 1.2.2 and Refs. [41, 42, 47]) until the next pulse comes along. Of course, at the excimer saturation density, the excimer density decays by exactly the factor 2^m between pulses. In the special case of counterflow, not only is the excimer density decreasing due to Penning ionization, but also due to the motion of the normal fluid removing them from the volume of helium that is illuminated by the laser pulses and introducing new, un-ionized helium atoms. At large enough flow velocities, it is possible that the steady state density reached at zero heat flux is simply unachievable. Empirically, we find that at a fs laser (rep-rate) of 1 kHz, the heat flux at which image quality is totally compromised is about 100 mW/cm^2 (6.44 mm/s). At higher rep-rates, we expect this heat flux to increase and, indeed, we find that at 5 kHz we can obtain high quality images up to heat fluxes close to (and sometimes exceeding) 400 mW/cm^2 (2.58 cm/s). Largely for this reason we choose to perform steady state counterflow visualization experiments with a fs laser rep-rate of 5 kHz.

2.2 Laser-field Ionization in Helium

Creating a usable excimer line in liquid or cold gaseous helium requires an understanding of how the ionization of atoms can occur. In the multi-photon regime, an atom is ionized when its outermost electron gains enough energy from incoming photons that the binding energy is exceeded. For helium, the ionization energy is 24.6 eV. If excimers were to be created in this way, each helium atom would have to be struck by about 16 photons with $\lambda = 800$ nm. Alternatively, in the tunneling regime, the electric field suppresses and distorts the coulomb potential, allowing the electron to simply tunnel from bound states to the continuum.

The transition between the two regimes is given by the Keldysh adiabaticity parameter [48]:

$$\gamma = \left(\frac{U_{ion}}{U_P}\right)^{1/2} = \left(\frac{U_{ion}}{e^2 F_0^2 / 2 m_e \omega^2}\right)^{1/2} \tag{2–2}$$

where U_{ion} is the ionization potential of the atom, and U_p is the ponderomotive potential of an electron in a laser electric field given by $F = F_0 cos(\omega t)$. When $\gamma \gg 1$ (high frequency, low field strength), multi-photon ionization is dominant, but when $\gamma \ll 1$ (low frequency, high field), tunneling ionization dominates. For atomic helium, the tunneling regime is only reached at laser intensities of $4 \cdot 10^{14}$ W/cm^2, well above the maximum energy flux achieved during the course of the experiments. Conversely, the multi-photon regime is reached below $4 \cdot 10^{10}$ W/cm^2, well below the energy fluxes in this experiment. However, for helium excimers, the ionization potential is low, 4.26 eV, so the tunneling ionization regime can be reached above intensities of $\sim 10^{12}$ W/cm^2. Thus, we require some population of He_2^* to already be present in fluid in order to allow the electron avalanche to occur. Possibly, this seed population can be generated by multi-photon ionization from the initial femtosecond pulse.

2.2.1 Ionization Threshold

We performed experiments to determine the ionization threshold of helium in order to confirm that our experiment functions in the way we would expect based on the theory of laser-field ionization. The ionization threshold experiments were done with the fs laser rep-rate set to 1 kHz. Since no fluorescence light is required, the experimental protocol is simpler than the description in § 2.1. We set exposure time to be 500 ms and collect light at each fs laser pulse. Each image is an average of 500 exposures. Fig 2-5 shows ionization lines in gaseous and superfluid helium. At a glance, it is clear that we can create a long, thin excimer line in superfluid helium as long as the laser energy remains below the breakdown threshold. Above the threshold, excimer clusters form, compromising the quality of the tracer line and making visualization experiments infeasible.

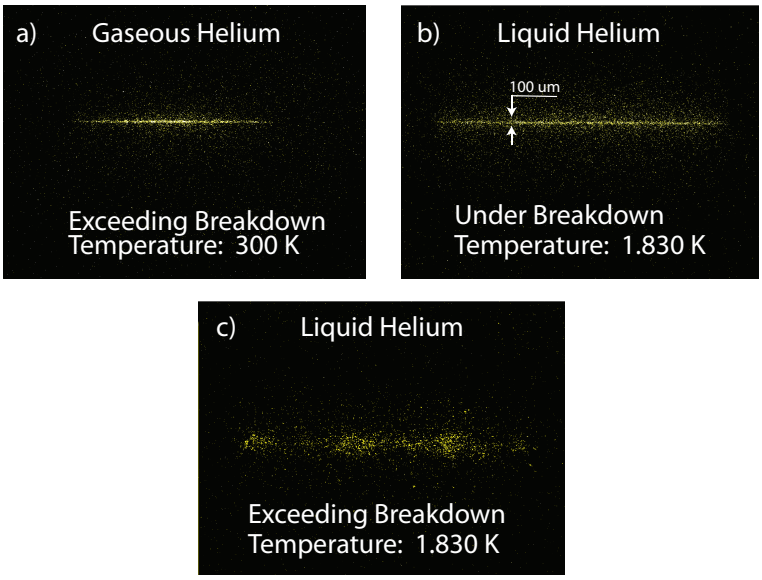

Figure 2-5: a) An averaged image of an ionization line in the multiphoton regime (gaseous helium, T = 300 K, P = 760 T). b) The ionization line in liquid helium, just below the breakdown threshold (T = 1.830 K). c) Clusters of ionization form in liquid helium when the femtosecond laser energy flux exceeds the breakdown threshold.

We collected such image data across a wide range of fs laser powers; from well below the ionization threshold to well above. We collected integrated intensity data in a region of interest defined as a small area around the ionization line, spanning the width of the channel. An example of such data for gaseous helium at 300 K and nearly atmospheric pressure is presented in Fig. 2-6. When plotted on a log-log scale, it is clear that the data follow two different power laws and thus indicate that there are two different light intensity regimes. We take the ionization threshold to be the 'kink' which marks the transition between regimes, which is determined by the intersection of the exponential fits (red lines).

The ionization thresholds calculated in this way are shown in Fig. 2-7 as a function of helium density (relative to the density of liquid helium, ρ_{LHe}). Black squares indicate data taken in the warm gas phase. The essentially constant nature of the ionization threshold exhibited in this density region is characteristic of the multi-photon ionization regime [49]. The red circle represents the ionization threshold in cold gas (13 K), and the blue triangle

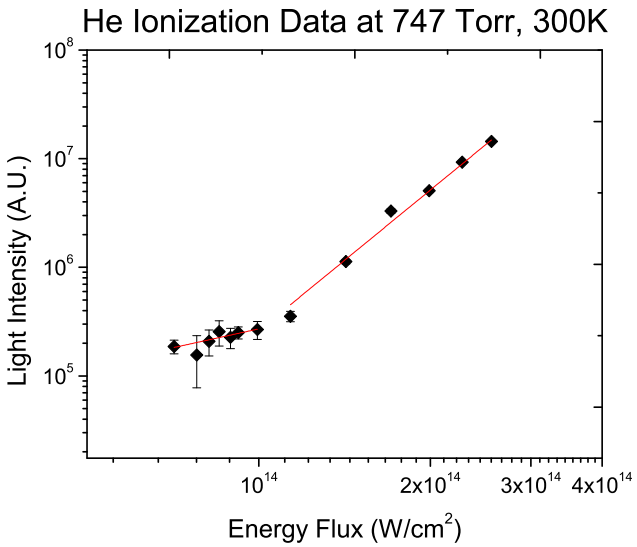

Figure 2-6: A representative data set of the ionization light intensity (in arbitrary units) in helium gas is presented as a function of the femtosecond laser energy flux. There are clearly two separate light intensity trends in the data shown by exponential fits (red lines). The transition from the slowly rising to rapidly rising regions is taken to be the ionization threshold. Each data point is an average of light intensity from ten images. The error bars indicate the light intensity fluctuations for each energy flux.

is ionization threshold in superfluid helium (1.830 K). That the ionization threshold falls by nearly an order of magnitude as density approaches ρ_{LHe} suggests that in cold gas and liquid helium, the ionization is caused by a controlled electron-avalanche cascade. Further, this observed ionization regime change is consistent with the work of Benderskii et al. [41].

2.2.2 Laser-induced heating

Another issue pertinent to the LIF visualization technique is the possible heating of the fluid due to the femtosecond and imaging lasers. Fluid heating would, of course, cause thermal counterflow as the heat is dissipated. In an extreme case, it is easy to imagine that the lasers introduce such large heat loads that the excimer line is immediately distorted and no measurements can be performed.

Fig. 2-8 (a)-(c) shows that the excimer line broadens, but does not distort, over the course of 50 ms. We find that the broadening is consistent with the process of molecular

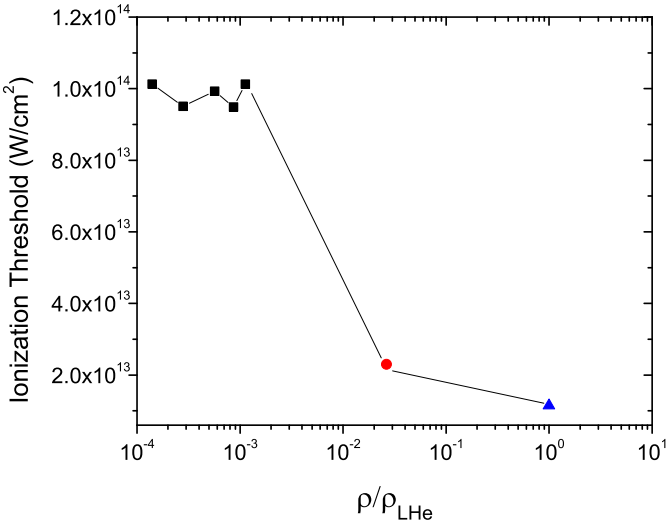

Figure 2-7: Ionization threshold of helium as a function of relative density. The black squares are ionization thresholds in warm gas, the red circle is ionization threshold in cold gas (13 K) and the blue triangle is the ionization threshold in helium II (1.830 K). In the warm gas, or at densities $\ll \rho_{LHe}$, the ionization threshold remains largely unchanged, which suggests ionization is occurring in the multiphoton regime. As density approaches that of liquid helium, the ionization threshold drops by a factor of 6.

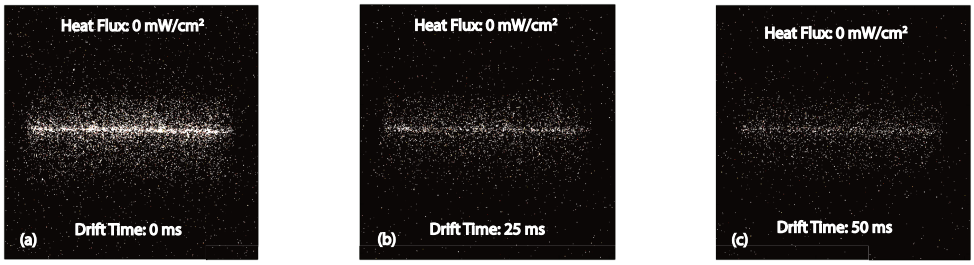

Figure 2-8: Single shot images of the excimer line under 0 mW/cm^2 heat flux. The image is taken (a) immediately after the fs laser passes through the channel; (b) 25 ms after the excimer line creation. The line is dimmer and more diffuse, but is at the same position as in (a), with no distortions; (c) 50 ms after excimer line creation. Still dimmer, but with no relative movement of any portions of the line.

diffusion, thus we conclude that the effect of laser heating will play no role in subsequent experiments.

2.2.3 Second Sound

Although most of this dissertation is concerned with the visualization of normal-fluid turbulence, it is nevertheless interesting and important to couple information about the normal fluid with the behavior of the superfluid under the same conditions. To this end, second sound resonances in the channel are excited (and detected) by oscillating superleak transducers [50]. Fig. 2-9 shows a diagram of the transducer design. The pore size of the membrane is 0.2 μm and the channel-facing side of the membrane is coated with 200-500 Å of gold.

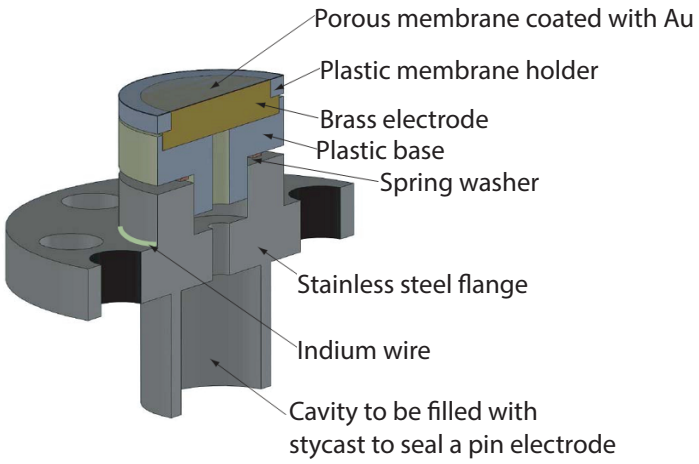

Figure 2-9: A cross-sectioned diagram of the 2^{nd} sound transducer (designed by Wei Guo with the assistance of Gary Ihas) to be mounted below the visualization cube. The gold-coated (200 to 500 Å) microporous (0.2 μm) membrane is stretched taut on the plastic membrane holder. When the brass electrode is biased with a voltage between $50-150$ V, the membrane is pulled toward the electrode. Oscillations of the membrane are then produced by an oscillating drive voltage from a function generator. Such a transducer can function as an emitter or receiver of 2^{nd} sound waves. This design deviates from the original design presented in Ref. [50] in that we have added a plastic base supported by spring washer, all set into a stainless steel flange that is to be sealed to the channel with an indium o-ring. The advantage of such a design is that, in principle, it is entirely reusable.

Fig. 2-10 demonstrates the electronics setup for the 2^{nd} Sound experiments. Both emitting and receiving transducers are biased at 50 V with a 6 V peak-to-peak drive

voltage applied to the emitter by the function generator. Capacitors are added to block DC signals from the low-level electronics. The detected waveform is sent to a Stanford Research Systems 830 lock-in amplifier, which then amplifies the signal and displays it via LabView.

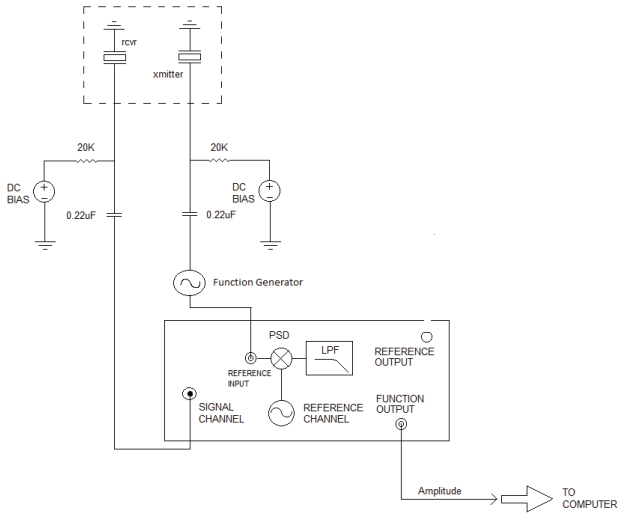

Figure 2-10: A diagram showing the configuration of the 2^{nd} sound generation/detection electronics. Each transducer (labelled 'rcvr' for receiver and 'xmitter' for transmitter) is given a DC bias between 50 - 150 V. The more sensitive electronics, namely the Stanford Research Systems model 830 lock-in amplifier and also the function generator are protected from unexpected voltage spikes from the voltages sources by two 200 nF capacitors. The function generator drives the transmitting transducer with a sinusoidal voltage waveform with peak-to-peak voltage of 2 V in order to excite 2^{nd} sound resonances. The function generator is, of course, also providing the reference signal used by the lock-in to detect the oscillated voltage from the receiving transducer. The detected resonance is then queried by a Lab View program and written to a text file stored on the data acquisition computer.

The 2nd sound attenuation experiments are performed in the following way. First, the function generator is set to sweep a large range of frequencies, from the fundamental frequency of the channel to about 40 kHz to find a resonance peak with the largest quality factor (Q) and good symmetry, which corresponds to largest sensitivity to vortex line density. Fig. 2-11 shows a portion of the frequency sweep from 15 kHz to 30 kHz. We find that, generally, resonance peaks with the largest Q ($\sim$ 600) are found between 19-26 kHz.

Once a candidate peak is identified, we set the frequency generator to make constant sweeps of width 600 Hz centered around the resonance frequency of the peak. The chosen width must include a flat region between resonance peaks, so that peak amplitude can be reliably calculated while at the same time minimizing the length of data collection. Due to the temperature dependence of the 2^{nd} Sound velocity, temperature fluctuations alter the fundamental resonance frequency of the channel. Although this frequency shift may be small for the fundamental, the shift is multiplied by the harmonic number for higher resonances. Thus for our experiments near 20 kHz, frequency shifts in the fundamental can have exaggerated results. Due to excellent temperature control in the cryostat, peak shifts due to temperature fluctuations are held to no more than 4 Hz at 20 kHz at T = 1.830 K. Data is only collected in this way after the heater has been active for 60 s or more, to ensure fully developed counterflow in the channel. Between each data set, we collected a 'baseline' measurement at zero heat flux to check for remnant vorticity and control for anomalous baseline shift.

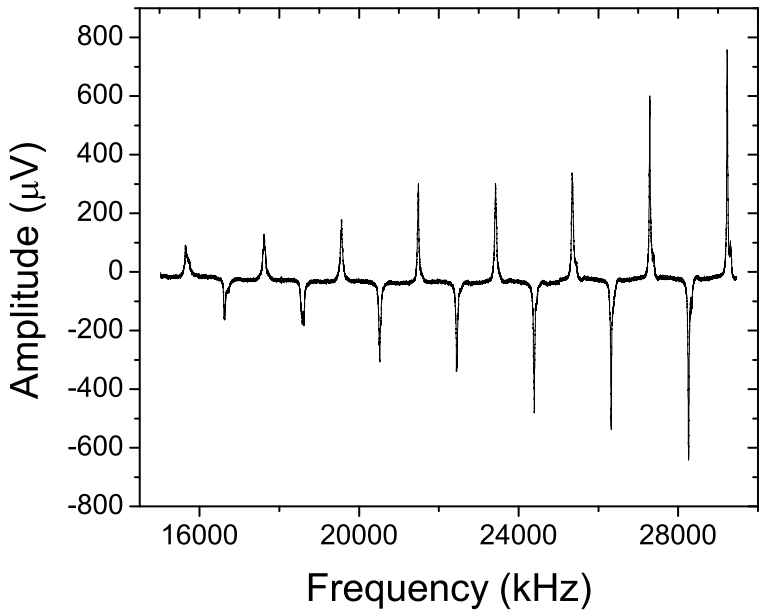

Figure 2-11: A sweep of 2^{nd} sound resonances from 15 kHz to 30 kHz. We find that, although the Q may be quite high close to 30 kHz, a shoulder begins to appear in the peaks. Additionally, peaks at such high frequencies exhibit ever greater frequency shifts due to temperature fluctuations. We find that the best compromises between resonance frequency and Q factor are those between 19-26 kHz.

CHAPTER 3
DATA ANALYSIS

This chapter presents the data analysis algorithms and considerations for the data collected in both the LIF and 2^{nd} sound attenuation portions of the experiment described in Ch. 2. The first portion, § 3.1, deals with the subtleties of analyzing LIF images in a real, experimental environment. Confounding factors such as light reflection from the channel walls, dark currents and the effect of the fluid velocity on excimer density are discussed. Then, an algorithm that can ameliorate the effects of the aforementioned difficulties while calculating velocity statistics is briefly sketched out. Section 3.2 describes the statistics performed on the attenuated 2^{nd} sound resonance peaks to calculate a vortex line density from the available data.

3.1 Image Processing Algorithm

A reliable and well-considered scheme for image processing is critical for experiments of this nature. The raw data comes in the form of a 1024x1025 matrix of integers. The ICCD camera itself has a resolution of 1024x1024, but an extra column is appended to number the rows. The following chapter describes the sequence of the image processing algorithm: binning, Gaussian fitting, comparison to baseline and generation of the relevant values (velocity profiles, structure functions, velocity PDFs, etc). The algorithm described in this chapter was developed entirely by Jian Gao as a part of his PhD work under the supervision of Dr. Wei Guo of the Florida State University Mechanical Engineering Department and National High Magnetic Field Laboratory.

Image processing starts with binning of the image . Since the channel fills approximately 80% of the field of view (FOV) of the CCD (about 800 pixels), generally the first 100 and last 100 pixels (px) can be discarded, since they do not contain any excimers. The remaining pixels will be divided into 32 px bins and the pixels are summed across their rows in each bin. Fig. 3-1 (a) shows a sample image, with one exaggerated bin designated by the dashed yellow lines. Fig. 3-1 (b) shows the subsequent step, in which the intensity

of each bin must be fitted to a Gaussian in order to determine the position of the excimer line segment in each bin. When the image in question is of an excimer line at nearly 0 s drift time and 0 mW/cm^2 heat flux, it is a comparatively simple task to find the excimer line with a Gaussian fit. However, most images will be taken at many tens of ms, with heat fluxes as large as 400 mW/cm^2, which can introduce several confounding factors. For instance, at large drift times, Penning-Ionization rapidly decreases the excimer density(see § 1.2.2 and Ref. [43]), which is demonstrated by the significantly attenuated fluorescence light intensity. Similarly, at large heat-fluxes, the saturation density of molecules might be decreased, which also will decrease fluorescence light intensity (see discussion of excimer creation near the end of § 2.1). Further, dark currents, which are present in all CCD cameras, and reflections of the fluorescence light from the back of the channel, may combine with the aforementioned effects to create images where the location of the line may not be obvious, especially to a computer. It is possible to empirically determine the mean light intensity emitted by the excimer line under the most favorable conditions (0 s drift time, 0 mW/cm^2 heat flux). With this value in mind, it is then possible to eliminate pixels containing counts that are significantly larger than the mean. Additionally, particularly bright pixels that are far from the experimental region (generally, the excimer line does not drift more than a few hundred pixels) can also be eliminated.

Subsequently, the bins can be summed across the columns to further increase the signal-to-noise. The Gaussian fit on each bin then determines the excimer line location and line width in the bin. If the light intensity in a certain section of the image is too low to produce a reliable Gaussian fit, that section can simply be omitted. As long as there are not too many such sections, the statistics of the image analysis do not suffer significantly. Every 10 images are matched with a corresponding baseline image (taken at 0 ms drift, 0 mW/cm^2 heat flux) in order to hedge against any gradual baseline shifts. Each section is either assigned as a baseline value, if it comes from a baseline image, or it

is compared to the relevant baseline section to determine a displacement. In this way we can calculate up to 6000 velocities from a set of 200 images. Expressions for mean velocity, u_{mean}, velocity fluctuations, Δu, and turbulent intensity I are given by

$$u_{mean} = \frac{1}{N}\sum_{n=1}^{N} u_n \qquad \Delta u_n = u_n - u_{mean} \qquad I = \frac{(\overline{\Delta u^2})^{\frac{1}{2}}}{u_{mean}}$$

where u_n is the velocity in bin n, N is the total number of bins or line segments, Δu_n is the velocity fluctuation in bin n, and the bar on $\overline{\Delta u^2}$ indicates an average over N line segments. The results of these calculations are plotted in Ch. 4.

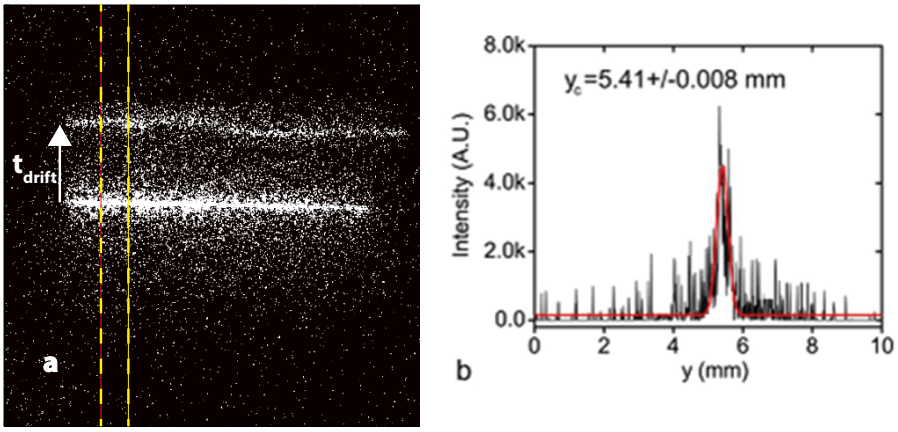

Figure 3-1: Binning and fitting of the capture image. (a) Shows a baseline image (200 mW/cm^2, 0 ms drift) with a distorted line overlay (200 mW/cm^2, 40 ms drift). The distorted line has been offset upward to provide an exaggerated comparison to the baseline. The dashed vertical yellow lines indicate the width of a bin, also highly exaggerated for clarity. The position of the distorted line segment found in the bin is compared to the position of the baseline segment located in the bin. The displacement is divided by t_{drift} to calculate the velocity of the line segment. (b) A representative sample of the Gaussian fits of the light intensity in each 32px bin. The center of the Gaussian is taken to be the position of the line segment (converted from pixels to mm) while the FWHM is taken to be the width of the line.

The structure function is a calculation of the velocity increment between any two points in the fluid. In the transverse case, we choose two different points located on the excimer line. In the longitudinal case, we would calculate the velocity difference between the same excimer line segment on two different excimer lines separated by some distance r. We are interested specifically in the second order structure functions primarily because,

under the right conditions, the exponent of the second order structure function can be simply related to the exponent of the energy spectrum. Specifically, if the energy spectrum has form $E(k) \propto k^{-p}$ where $1 < p < 3$, then the second order structure function must have form $S_2(\vec{r}, \vec{R}) \propto r^{p-1}$ and the transverse component of $S_2(\vec{r}, R)$ must also behave as r^{p-1} (a derivation of this relation can be found in Ch. 4 of Ref. [46]). The equation for transverse structure functions of order n, $S_n^{\perp}(r, R)$, is given below.

$$S_n^{\perp}(r, R) = \langle [u\,(R + r/2) - u\,(R - r/2)]_{\perp}^n \rangle = \langle [\delta u_{\perp}(r)]^n \rangle \tag{3–1}$$

R is the location of the reference point, r is the distance between the two velocity segments in question, u is the velocity of the segment, n is the order of the structure function, and the angle brackets indicate an average over many trials.

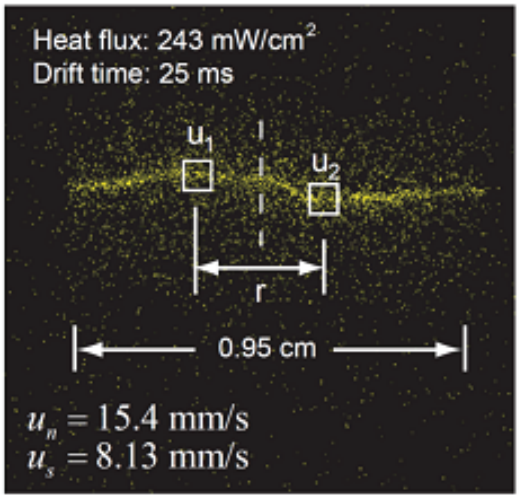

Figure 3-2: A single shot image of the excimer line under a heat flux of 243 mW/cm^2 after drift time of 25 ms. The normal fluid velocity $u_n = 15.4$ mm/s upward and superfluid velocity $u_s = 8.13$ mm/s downward. The vertical dotted line shows the position of the reference, R, while the boxes indicate which velocities (u_1 and u_2) are to be compared in the structure function calculation. The segments of the line to be compared are found by choosing r and moving distance $r/2$ either left or right from the reference point.

Fig. 3-2 demonstrates one instance of the structure function calculation. The reference point is taken to be at the center of the excimer line. In Fig. 3-2, u_2 is $u\,(R + r/2)$ and u_1 is $u\,(R - r/2)$, since the origin is defined to be in the bottom right

corner. Since turbulence is a random phenomenon, we can immediately conclude that odd-order, transverse structure functions must be be identically zero. In light of this, we calculate only the second-order, transverse structure function. By moving the reference point (usually at the center of the excimer line) to different positions along the excimer line, we can check whether the turbulence is homogeneous. Of course, the statistical weighting for points with a separation, r, close to the channel width is much smaller than for points on the line with small separation.

3.2 2nd Sound Attenuation

The 2^{nd} sound experiments are performed as described in the previous chapter. We collect data points at a rate of 10 points per second over the course of 62 s. Each such scan over a resonance peak has width 600 Hz to ensure peak and baseline are captured. 600 Hz is much wider than the FWHM of the resonance peak, even when it is strongly attenuated by the presence of vortex lines. Each experimental run sweeps frequencies over the same peak about 20 times. Zero heat flux data is collected between each non-zero heat flux to avoid the effects of possible baseline shifting. The resonance peak and left (or right) baseline is collected by a program that iterates through each data file. For heat fluxes in excess of $\sim$ 60 mW/cm^2, it is sufficient to average peak heights to find the attenuation of the 2^{nd} sound signal. However, at heat fluxes $<$ 60 mW/cm^2 the attenuation is small enough that a sample size of 20 produces extremely large error bars. In such cases, each non-zero heat flux amplitude is subtracted from each zero heat flux baseline amplitude. Analyzing the data in this way allows for better statistics in the very low heat flux regimes.

Fig. 3-3 compares an unattenuated 2^{nd} sound resonance peak (collected at 0 mW/cm^2) with an attenuated peak collected at 300 mW/cm^2 heat flux. Recall that the vortex line density as a function of attenuation was given by equation (1–11):

$$L = \frac{6\pi\Delta}{\kappa B}\left(\frac{A_0}{A} - 1\right)$$

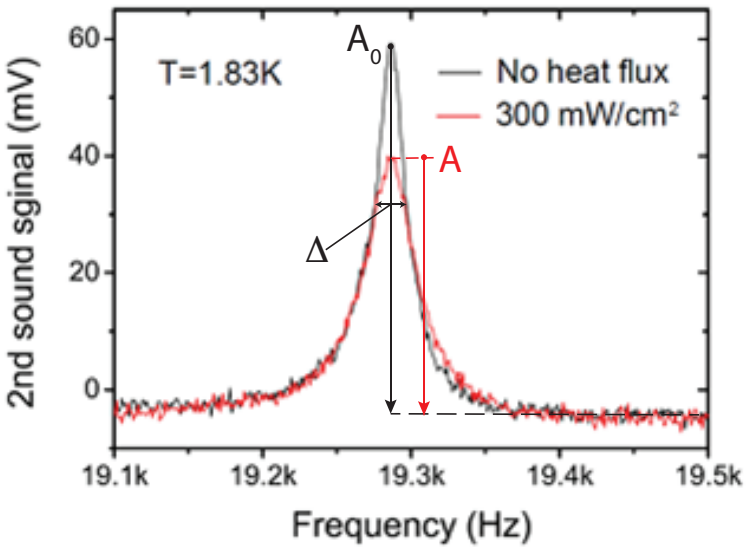

Figure 3-3: A comparison of the unattenuated 2^{nd} sound resonance at $\sim$ 19.3 kHz to the same resonance collected under steady state counterflow conditions generated by a heat flux of 300 mW/cm^2. The black arrow marked by A_0 indicates the unattenuated resonance amplitude, while the red arrow marked by A indicates the attenuated amplitude at the aforementioned heat flux, and Δ denotes the FWHM of the unattenuated peak. The measured attenuation in this case is about 33%. Additionally, it is clear that the the wave form is not significantly affected by the vorticity in the channel, nor should we expect any significant baseline shifts in the experiment.

where A and A_0 are the attenuated and unattenuated amplitudes, respectively. Δ is the FWHM of the unattenuated peak, κ is the quantum of circulation ($\hbar/m_4$) and B is the mutual friction coefficient. The unattenuated amplitude (A_0) and attenuated amplitude (A) are both shown in the figure using the right side of the resonance as a baseline.

CHAPTER 4
STEADY STATE COUNTERFLOW

This chapter will present and discuss the data collected over the course of the experiment. The results that follow can be found in an extremely abbreviated form in reference [51]. Section § 4.1 consists largely of images taken in fully turbulent counterflow. § 4.1.1 presents velocity probability functions and the mean velocity as a function of heat flux and the turbulence intensity of the fully turbulent normal fluid. § 4.1.2 presents structure functions computed across a wide range of heat fluxes and their corresponding energy spectra power laws. It will be shown that the energy spectrum has a non-classical power law, apparently indicative of quantum turbulence. Finally, § 4.2 presents the excimer line distortion in what we term the distorted laminar region and presents some preliminary evidence that this distortion is related to the TI/TII (see § 1.1.3) transition in the superfluid component.

4.1 Fully Turbulent Flow

Fig. 4-1 shows the distortions of the excimer line in fully turbulent flow conditions. Fig. 4-1 (a) shows the baseline image under 0 mW/cm^2 heat flux and 0 ms drift time. Fig. 4-1 (b) - (d) show the random distortions of the excimer line under fully-turbulent thermal counterflow conditions. Indeed, such conditions will be the focus of this section.

4.1.1 The Normal Fluid Velocity

Fig. 4-2 shows the mean normal fluid velocity, u_{mean} as a function of heat flux. The flow velocity, u, is calculated as described in Ch. 3. Each open circle datum is the average of u over the excimer line and approximately 200 single-shot images under the relevant counterflow conditions. The first 5 data points are obtained in the laminar (open red triangle) and distorted laminar (open square) regions. The solid black line is the normal fluid velocity given by equation (1–9) [52]

$$v_n = \frac{q}{\rho s T}$$

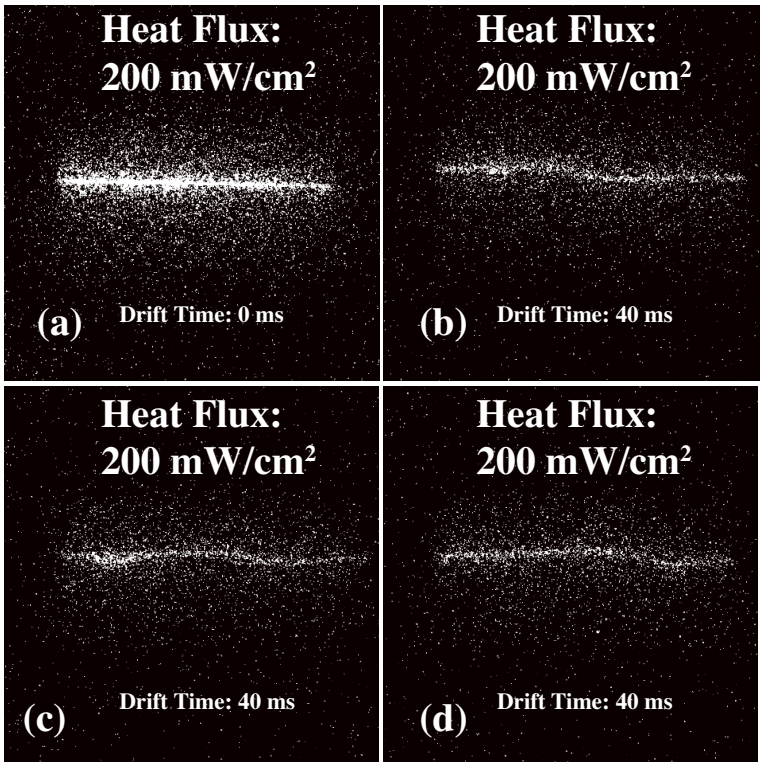

Figure 4-1: Images of the excimer line under a variety of steady-state counterflow conditions. (a) A baseline image at 200 mW/cm^2 and 0 ms drift time. The line is measured to be 110 μm wide and 9.5 mm long. (b) - (d) Single-shot image of the excimer line distortion at a heat-flux of 200 mW/cm^2 and 40 ms drift time. We expect this heat flux to be firmly in the fully-turbulent regime, and the random distortions of the line support this expectation.

where q is the heat flux, v_n is the normal fluid velocity, ρ is the density of the fluid, s is the entropy per unit mass and T is the temperature of the fluid. The error bars in the fully turbulent regime are the averages $\overline{(\Delta u^2)}^{1/2} = \langle\overline{(u - u_{mean})^2}\rangle^{1/2}$, which represent the magnitude of the velocity fluctuations. As expected, they become more extreme as heat flux increases. Since all of the data in Fig. 4-2 lie along the line described by (1–9), we consider this confirmation that the helium excimers are well-coupled to the normal fluid.

With the velocity data extracted from the images, we can also calculate the turbulence intensity of the flow, given by $\frac{\overline{(\Delta u^2)}^{1/2}}{u_{mean}}$. Again, each datum is calculated from an average over the length of the excimer line in 200 images. From the data, it is clear the turbulence intensity is more or less independent of heat flux up to 350 mW/cm^2,

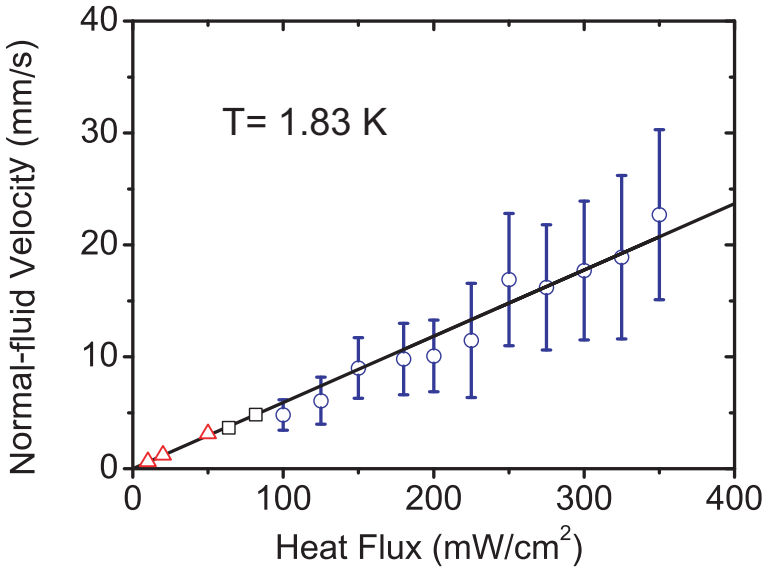

Figure 4-2: Normal fluid velocity as a function of heat flux ($\dot{q}$). The open red triangles denote velocities obtained during fully laminar flow, the open black squares are velocities obtained in the distorted transition regime and open blue circles are velocities in the fully turbulent flow. The solid line is a plot of (1–9) and the error bars indicate the magnitude of velocity fluctuations in the flow. The data clearly show that the excimers are well-coupled to the normal fluid [51].

beyond which it becomes impossible to produce high quality single-shot images of the distorted excimer line. In classical fluids, the turbulence intensity in simple geometries, such as a channel with square cross-section, is consistently found to range between 1% and 5%. Notably, the turbulence intensity we observe in superfluid helium is nearly 30%, significantly higher than in a classical fluid. Although this is a real, reproducible effect, as yet there have been no clues as to why exactly this should be the case. It may be interesting to note that the calculated turbulence intensities plotted in Fig. 4-3 assume that the relevant mean velocity is the velocity of the normal fluid, v_n. However, if the relevant mean velocity is the counterflow velocity, $v_n - v_s$, then we find that the turbulence intensity drops to 20%.

A representative sample of the velocity probability density functions (PDFs) is presented in Fig. 4-4. In each instance, the red line represents a fit of the data to a Gaussian distribution. It is apparent that the velocity distribution is very close to

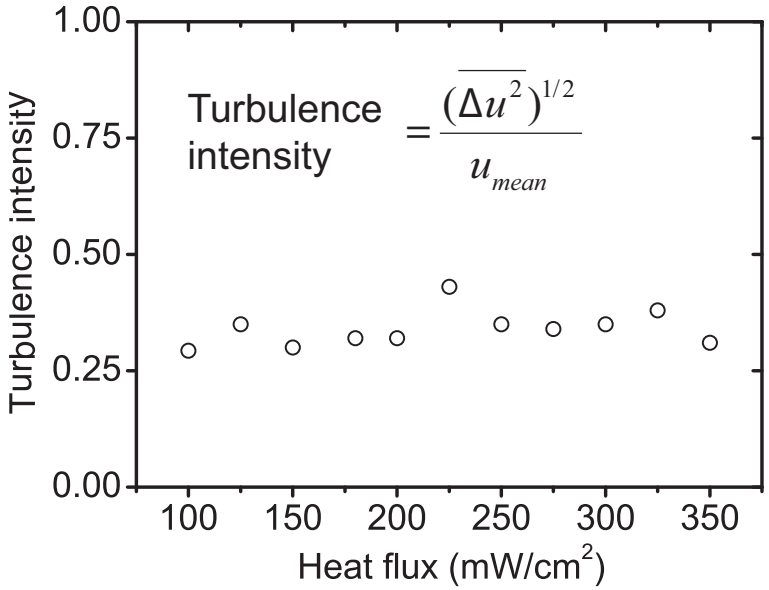

Figure 4-3: Turbulence intensity plotted as a function of heat flux, $\dot{q}$. As expected, the intensity is approximately constant across the entire range of usable heat fluxes. Note, however, that the magnitude of the turbulence intensity in superfluid ^{4}He (30%) is much higher than in a classical fluid, which is $\sim$ 5% . Although this effect is real and reproducible, it is unclear why the turbulence intensity for helium II should be so much higher than in classical fluids [51].

Gaussian for all heat fluxes. (The plots in Fig. 4-4 are reproduced somewhat larger in the Appendix along with additional velocity PDF plots at heat fluxes in between those of Fig. 4-4). Furthermore, the power law tails reported in the experiments of Ref [53] and attributed to vortex line reconnections are not present in our data. This does not necessarily suggest that these tails do not exist. Based on the viscous relaxation time (see Eq 1–13), we can be very sure that the excimers are well coupled to the normal fluid, not vortex lines. However, the normal fluid near the locations of vortex line reconnections can, briefly, have a very high velocity due to the mutual friction, which then contributes to the formation of power-law tails. On short probing time scales, these high velocities should be observable. However, at the comparatively long time scales ($\sim$ 10 ms) in this experiment, the excimers have time to move away from these high velocity regions and exhibit a normal velocity.

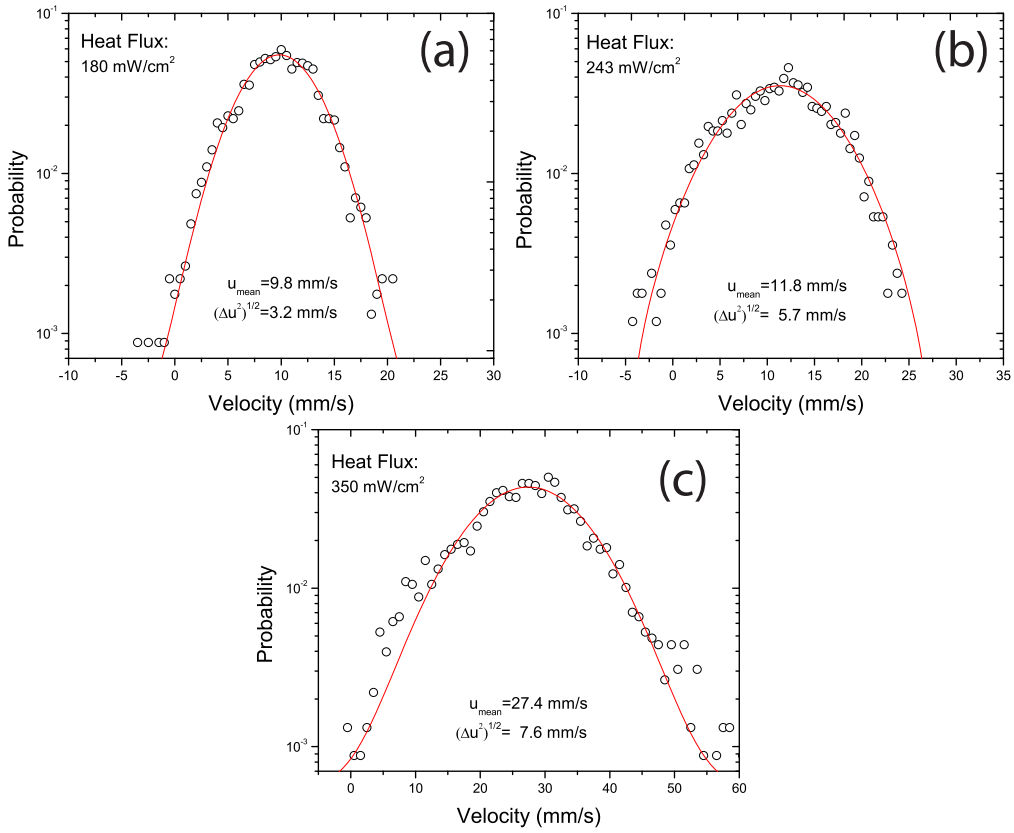

Figure 4-4: The velocity PDFs are shown for steady state thermal counterflow with heat fluxes (a) 180 mW/cm^2, (b) 243 mW/cm^2 and (c) 350 mW/cm^2. Each PDF is shown with a Gaussian fit (red line), which matches the data closely in each case. The calculated mean flow velocity and RMS velocity fluctuations are displayed. The mean velocity values agree well with (1–9).

4.1.2 The Second Order Transverse Structure Function

With knowledge of the excimer line segment velocities, we calculate the second-order, transverse structure function as described in § 3.1. Fig. 4-5 presents $S_2^{\perp}$ as a function of horizontal distance, r, on the excimer line. We find that, in fully turbulent, steady state thermal counterflow, $S_2^{\perp} \propto r^n$, where $n = 1 \pm 0.05$[51] independent of heat flux for $r < 2$ mm. Additionally, for r smaller than the size of the channel, we find no dependence of the calculated structure functions on the reference coordinate, R, which suggests that the normal fluid turbulence is homogeneous at these length scales. While the calculated structure function for large r also appears to be independent of the location of

the reference point, the statistical weighting for these values is much smaller, since only one or two values of $S_2^{\perp}$ can be extracted at $r \sim 1$ cm. Thus, we cannot be certain of the homogeneity of the turbulence at large scales ($r \sim 1$ cm). The behavior of the 2^{nd} order, transverse structure function in steady state counterflow strongly suggests that the character of counterflow turbulence is non-classical at all probed length scales.

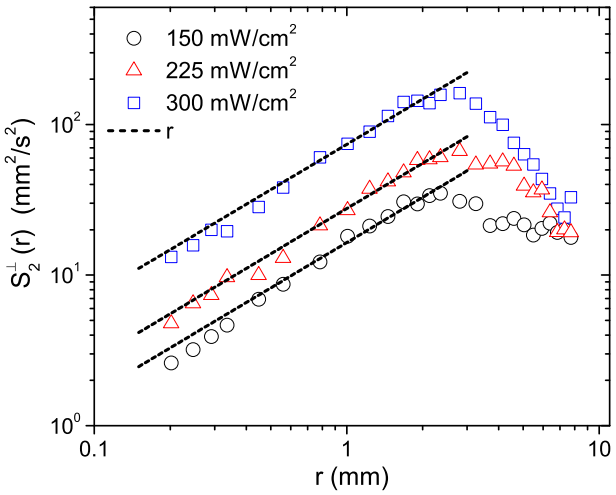

Figure 4-5: A plot of the transverse, second-order structure function at 150 mW/cm^2 (open green circles), 225 mW/cm^2 (open red triangles) and 300 mW/cm^2 (open blue squares). The black dotted line over-lay on each of the data sets is a plot of r^1. The power law of the second-order, transverse structure function is then calculated to be $S_2^{\perp} \sim r^1$, which corresponds to an energy spectrum power law of $E(k) \sim k^{-2}$ [51].

In classical turbulence, far from boundaries, we expect that the structure function of the turbulence will level off as the separation distance r exceeds the size of the energy containing eddies and the velocities become uncorrelated. Experiments using the RELIEF tagging method in a supersonic jet of air find that jet flow exhibits features of homogeneous turbulence. That is to say, the second order transverse structure function has form $S_2^{\perp}(r) \propto r^{2/3}$, which corresponds to energy spectrum $E(k) \propto k^{-5/3}$ [54]. Both of these exponential forms correspond to classical, Kolmogorov turbulence. Although such experiments have been done for channel flow (using the a related molecular tagging technique: PHANTOMM), the region of interest was small and far from boundaries [55].

The behavior of the structure function in classical turbulent channel flow near the walls is still not obvious. However, numerical evidence suggests that the value should increase due to increase in the mean shear [56].

Since the structure function has form $S_2^{\perp} \propto r^n$, where n is 1, we are able to immediately deduce the power law of the energy spectrum: $E(k) \propto k^{-2}$ (see the structure function discussion in § 3.1). Indeed, it is possible to determine the full form of the energy spectrum from the structure function data, but the process is non-obvious and non-trivial. Knowing the power of the energy spectrum in the cascade region was sufficient for these experiments, but there is current work being performed to determine the exact energy spectrum and its consequences for counterflow turbulence [57]. A classical, $E(k) \propto k^{-5/3}$, (Kolmogorov) power law would imply that both fluids move as one, classical fluid. Indeed, this occurs after the counterflow is allowed to decay for sufficient time (some evidence of the decaying thermal counterflow structure functions is provided in Ref. [51]). The experimental setup described in Ch. 2 can be used to probe the behavior of the normal fluid in decaying counterflow, but a detailed discussion of such experiments is outside the scope of this dissertation. That we observe a non-Kolmogorov energy spectrum in steady state counterflow suggests that the turbulence is indeed non-classical. In such non-classical turbulence, energy is expected to be dissipated in a wide range of the available length scales due to the mutual friction between normal and superfluid components.

4.2 Laminar, Distorted Laminar Flow and the TI/TII Transition

Fig. 4-6 shows the deformation of the excimer line starting in the laminar flow regime and progressing through what we have termed the distorted laminar flow regime. Each image after the initial, undistorted baseline is a nine-shot average which both emphasizes the consistency of the central parabolic structure and improves the signal to noise ratio in the image at drift times $\geq$ 100 ms. The flattening of the edges of the excimer line begins near 55 mW/cm^2, but is presented here at higher heat fluxes to unambiguously display the phenomenon.

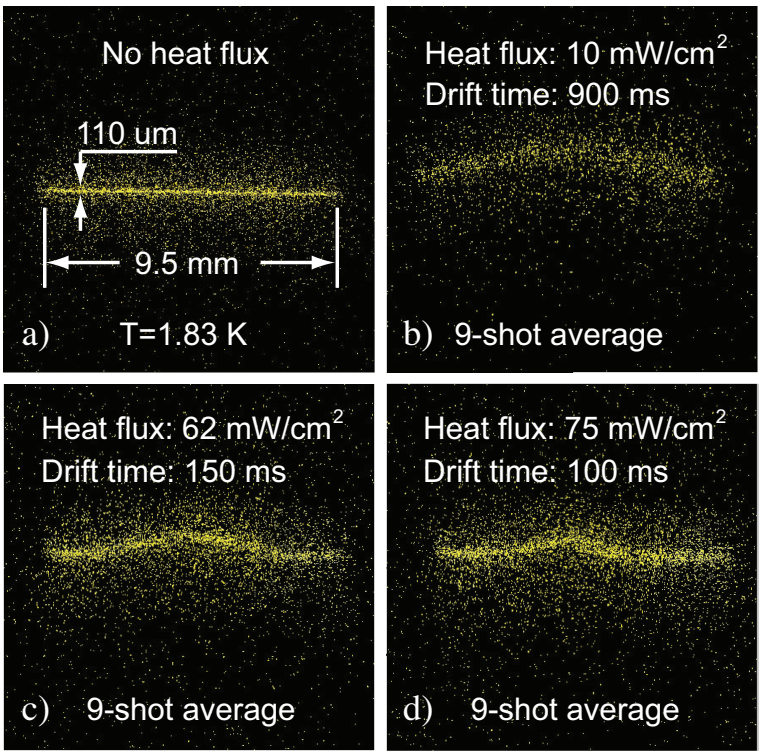

Figure 4-6: The distorted laminar region in steady state counterflow. (a) The excimer line before the heater is activated. b) A nine shot average of the line at 10 mW/cm^2 and 900 ms drift time. From the parabolic distortion of the line, we conclude that the flow is laminar. c) A nine-shot average of the excimer line distortion at 62 mW/cm^2 and 150 ms drift time. Note that the center of the line is distorted in a way that suggests laminar flow, but the edges of the excimer line have begun to flatten out. d) A nine-shot average of the excimer line distortion 75 mW/cm^2 at 100 ms drift time. At this point, there is still some laminar distortion in the center of the excimer line, but much of the line has become flattened out.

Although Fig 4-6 (b) certainly appears to be laminar, it is preferable to provide some quantitative evidence to that effect. Fig.4-7 shows an averaged image of the excimer line under flow conditions we expect to be laminar ($\dot{q}$ = 20 mW/cm^2, u_n = 1.29 mm/s) and the corresponding fit of the excimer line velocity to a parabolic velocity profile. We find that the empirically determined mean velocity is consistent with the normal fluid velocity calculated from (1–9) and, further, that the velocity at the center of the excimer line is twice that of the mean, which is consistent with Poiseuille flow.

Having confirmed that thermal counterflow produced by low heat fluxes ($<$ 50 mW/cm^2, $<$ 3.23 mm/s) results in a laminar normal fluid flow profile, we now turn our attention

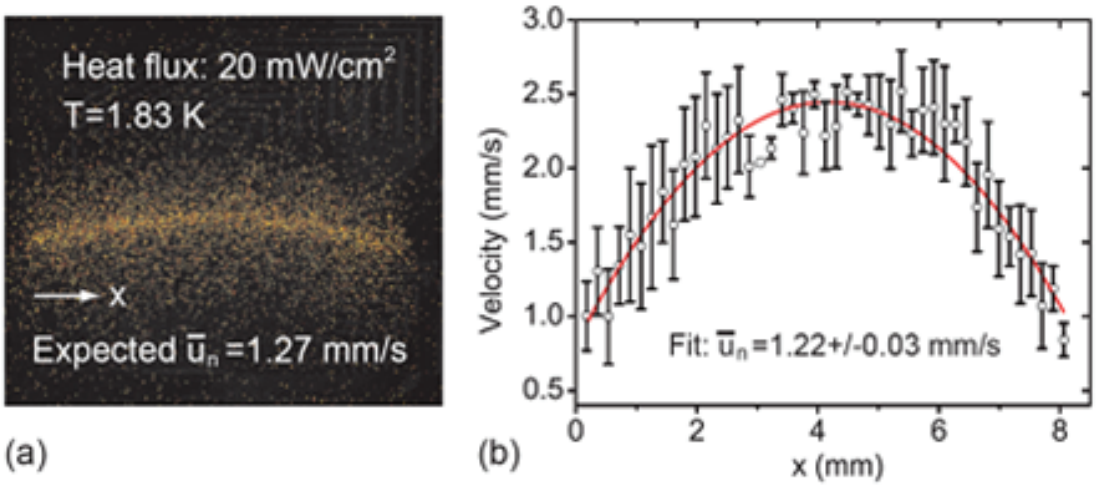

Figure 4-7: A quantitative analysis of low heat flux normal fluid flow. (a) Shows a 9-image average of the deformation of the excimer line at $T = 1.830$ K and a heat flux of 20mW/cm^2. The distortion of the excimer line appears to be laminar. (b) Shows a parabolic fit of the excimer line velocity (determined from (a)) which yields the expected normal fluid velocity.

to the distortions in the laminar profile encountered between $50 - 80$ mW/cm^2 ($3.23 - 5.15$ mm/s). The flattening of the excimer line proceeds to increase until, at a heat flux of roughly 80 mW/cm^2 (5.15 mm/s), the central laminar region disappears entirely. The flat portions of the line in the distorted laminar regime are expected to actually be random distortions due to interactions between normal fluid and the vortex line tangle, but which are averaged out to a flat line due to the averaging of captured images. Above 80 mW/cm^2 (5.15 mm/s), it becomes possible to take single-shot images of the excimer line and random distortions are observed, confirming the transition to full turbulence. Fairly recent numerical studies [58–61] find that, under Poiseuille flow in a simple, square channel geometry, vortex line density initially accumulates near the walls. In light of these simulations, we then posit that the flattening of the excimer line is caused primarily by mutual friction interactions between the normal fluid and vortex lines near the walls of the channel. It is possible to exclude small-scale normal fluid turbulence as the cause of the excimer line flattening. Recent analysis of single-shot images taken in the laminar (40 mW/cm^2), distorted laminar (70 mW/cm^2) and fully turbulent flows

(150 mW/cm^2) with a fixed drift time of 100 ms indicate that the width of the line increases by $< 5\%$ from laminar to distorted laminar flows, but widens significantly ($\sim 14\%$) in fully turbulent flow [62]. Since the line width in the distorted laminar flow is consistent with the expected width due to non-turbulent diffusion, small-scale normal fluid turbulence is ruled out as a cause of the line flattening shown in Fig. 4-6. If the distorted laminar region is caused by vortex line buildup near the walls of the channel, then the increased average vorticity in the channel should be detectable in a 2^{nd} sound attenuation experiment. Furthermore, some numerical simulations [59] predict that the transition to full normal fluid turbulence should correspond to an abrupt increase in vortex line density. Similarly, earlier numerical work performed by Melotte and Barenghi [63] suggests that the transition from TI superfluid turbulence to TII superfluid turbulence is intimately linked to instabilities in the normal fluid. Now that the behavior of both the superfluid and normal fluid components can be reliably probed, we seek to test these predictions experimentally.

The work of Tough and Martin [14] is reproduced below in Fig. 4-8 to demonstrate the characteristics of the TI/TII transition. Although the data presented in Fig. 4-8 (a)-(c) are collected at significantly different temperatures, they demonstrate that the TI/TII transition occurs with reproducible characteristics. As expected, the initial line density is zero until the first critical velocity, v_{c1}, is reached, after which the line density increases slowly until the second critical velocity, v_{c2} is reached, at which time the line density jumps up and then smoothly settles into the behavior first measured by Vinen [15].

Calculating vortex line density from measurements of the temperature gradient necessarily required that all experiments that demonstrated a TI/TII transition in superfluid helium were performed in channels of width at least an order of magnitude smaller than the one described in § 2.1. The characteristic size of our channel is such that the temperature gradient in the channel would be below the resolution of the available

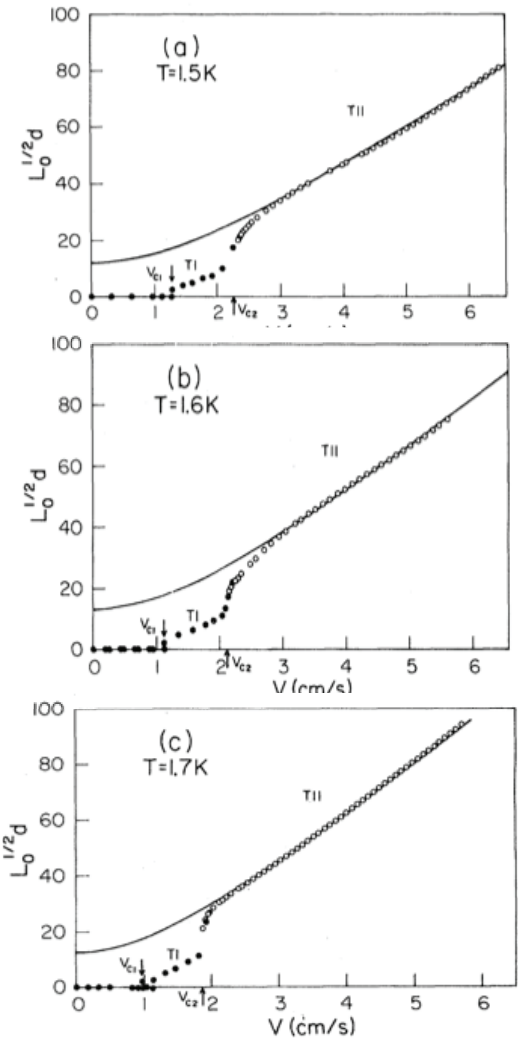

Figure 4-8: Figures reproduced from Ref [14] plotting a dimensionless quantity, $L_0^{1/2}d$ as a function of counterflow velocity, v_{ns}. (a), (b) and (c) show essentially the same behavior of the vortex line density, but at temperatures of 1.5 K, 1.6 K, and 1.7 K respectively, in a channel of characteristic size 1 mm. As counterflow velocity increases from zero, the line density is initially zero, begins to rise at the first critical velocity, v_{c1} and tends to increase abruptly at the second critical velocity v_{c2}. Reprinted Fig. 10 with permission from K. P. Martin, J. T. Tough, Phys. Rev. B 27 (1983), http://dx.doi.org/10.1103/PhysRevB.27.2788. Copyright 2015 by the American Physical Society.

thermometers. Conveniently, in large channels, the vortex line density can be probed by measuring the attenuation of standing 2^{nd} sound waves, the details of which are described in § 2.2.3. Fig. 4-9 (a) shows the square root of the vortex line density, $L^{1/2}$, as a function of heat flux, from the laminar through the fully turbulent regime. The red line represents

a fit to $L^{1/2} = \gamma(V_{ns} - V_c)$ and returns a γ value of 162 s/cm^2, which is consistent with previous 2nd sound measurements in the fully turbulent TII region. Fig. 4-9 (b) presents a close up of several experiments confined to heat fluxes which correspond to the laminar and distorted laminar regions in the normal fluid flow. At heat fluxes below about 55 mW/cm^2, the uncertainty on the measurements is equivalent to the measured values, but the distribution of $L^{1/2}$ values around 0 cm^{-1} suggests that this is below the first critical velocity. The next region, from 55 mW/cm^2 to 80 mW/cm^2 begins with a sharp jump in $L^{1/2}$, and subsequently demonstrates a small, positive slope that increases until it obtains the value for γ obtained in the fully turbulent regime ($\geq$ 80 mW/cm^2).

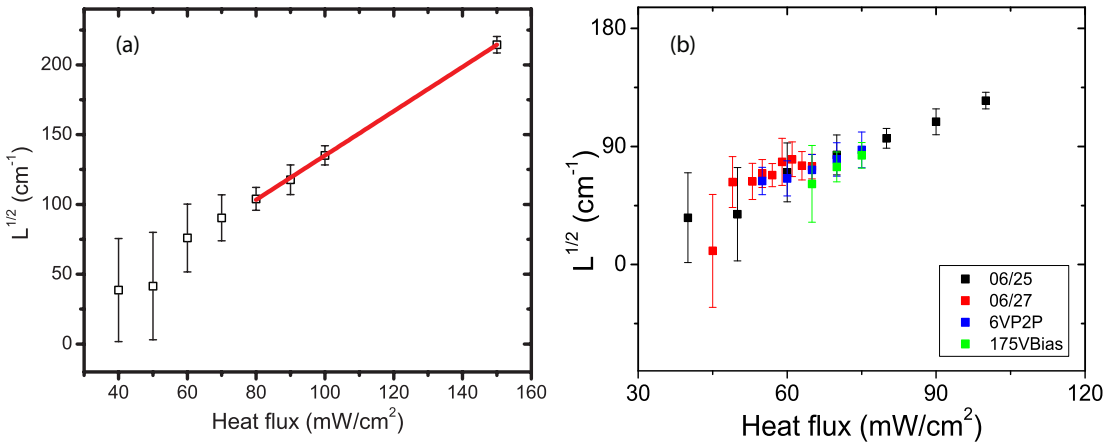

Figure 4-9: Square root of the vortex line density as a function of $\dot{Q}$. (a) The red line is a fit in the fully turbulent region to the equation $L^{1/2} = \gamma(V_{ns} - V_c)$. The fitted value of γ is 162 s/cm^2, which is consistent with previous work on superfluid turbulence. (b) focuses on the lower heat flux region, indicating that the data are repeatable, but the large error bars below 50 mW/cm^2 make it impossible to draw conclusions about the existence and size of the TI region. Note that error bars that extend below zero are not meant to suggest that the value of $L^{1/2}$ can drop below zero. [51].

A comparison with Fig. 4-8 suggests that the superfluid enters the TII turbulence state at 55 mW/cm^2 and, due to the large error bars, the TI region, if it exists, cannot be seen. It appears that an increasing vortex line density, and thus increasing mutual friction between the normal and superfluid components, contributes to normal fluid instability rather than the other way around as suggested by Melotte and Barenghi [63]. Further, it

is clear that there is no sharp jump in vortex line density at the point where the normal fluid becomes fully turbulent. This disagreement with numerical simulations is perhaps not very surprising. To date, no simulations of superfluid flow are self-consistent. That is to say, all simulations of superfluid flow normally enforce a single laminar or turbulent flow profile in the normal fluid, which is not permitted to evolve as a function of time. However, very recently, Yui and Tsubota have performed simulations which, though they are not self-consistent, allow for flattening of the Poiseuille profile. Their results present further evidence that tail-flattened flow or, as we call it, distorted laminar flow, is a flow state with characteristics between those of fully laminar flow and fully turbulent flow [64]. Given these latest advances, it is reasonable to expect that, with guidance from experimental results, future self-consistent simulations can reproduce known phenomena and provide further insight into quantum turbulence.

CHAPTER 5
CONCLUSION

The need for an effective, reliable tracer for the visualization of turbulence in superfluid flows has driven the development of an experimental apparatus which uses the excited helium dimer (He_2^*) as a tracer in the normal fluid, and exploits the available electronic energy levels of this molecule to perform laser-induced fluorescence visualization. We build upon previous work detailing the development of helium excimers as tracers [35, 37, 38] to create a system that generates and images a thin line of helium excimers in bulk liquid helium II flow. Conveniently, the vast majority of the experimental apparatus components are commercially available, the only custom machined components being the experimental channel itself and the 2^{nd} sound transducers. We present an initial investigation of the ionization threshold of ^{4}He as a function of density to characterize the width of the excimer line and determine the optimal operation parameters of the apparatus. We find that ionization light can be produced even at low helium densities (i.e. at STP) when ionization occurs entirely by the multiphoton mechanism. In the superfluid, we find that the excimer line has width $\sim$ 100 μm just under the breakdown threshold (60 μJ/pulse). Above the breakdown threshold, we see diffuse clusters of excimers form, but which are unusable for the visualization experiments to follow. The LIF experiments in steady state counterflow performed at 1.830 K spanned the range of heat fluxes from $0 - 350$ mW/cm,^{2} and revealed a number of interesting characteristics of normal fluid flow. The normal fluid does have a fully laminar regime below 50 mW/cm^2 ($v_n \leq 3.26$ mm/s). Unexpectedly, the laminar profile of the excimer line began to display a flattening (in averaged images) of the line near the experimental channel edges as the heat flux rose above 55 mW/cm^2 until the entire line was flattened above 80 mW/cm^2 ($v_n \geq 5.15$ mm/s. Some numerical simulations [58, 59, 61] indicate that there is a preferential buildup of vortices near the walls of the channel, which may suggest that line flattening in the distorted laminar region is due to the normal fluid interaction with these vortices. Very

recent experimental results rule out small-scale turbulence in the normal fluid as a cause of the flattening, lending more credence to the aforementioned numerical studies. These simulations also predict that the vortex line density jumps sharply when the normal fluid transitions to full turbulence. However, our experiments probing the vortex line density in the channel using the method of 2^{nd} sound attenuation find that the vortex line density increases smoothly from the start of the distorted laminar region through the transition to full turbulence and beyond. Furthermore, an attempt to experimentally investigate the numerical work of Melotte and Barenghi [63] regarding the relationship between normal fluid instability and the states of superfluid turbulence (TI and TII) met with extremely limited success. While it is clear that a TII turbulence state exists above 80 mW/cm^2, coincident with a fully turbulent normal fluid, the error bars on the 2^{nd} sound measurement at heat fluxes below 80 mW/cm^2 quickly become comparable to the magnitude of the attenuation, making definite statements regarding the TI state and the TI/TII transition impossible.

Disagreement with some of the predictions of Refs. [59, 61] likely stems from limitations of the simulations themselves, which are not self-consistent. These simulations define a flow profile for the normal fluid, either laminar or turbulent, but do not allow it to evolve while calculating the the evolution of the vortex tangle in the superfluid. Self-consistent simulations require a knowledge of the boundary conditions for superfluid flow in the presence of vortex lines that can be pinned to channel surfaces. Our work, especially in the distorted laminar region, can provide important empirical evidence against which simulations can be checked and correct boundary conditions selected.

The over-arching goal of this work, to capture high quality, single-shot images of normal fluid flow, is realized in heat fluxes above 80 mW/cm^2 (subsequent refinements to the apparatus extended this to the distorted laminar region as well). Calculating average velocities for the excimer tracers shows that the normal fluid velocity agrees well with the velocity predicted by Eq. 1–9, which suggests strong coupling between the normal

fluid and the excimer tracers. The normal fluid turbulence intensity, a measure of the root-mean-square velocity of the velocity fluctuations divided by mean flow velocity, shows no dependence on heat flux, but has value $\sim 30\%$ rather than the classical value of $(1\% - 5\%)$ found in simple flow geometries. The calculated velocity probability density function of the normal fluid flow is fitted well by a Gaussian function and displays none of the power-law tails observed in Ref. [53]. The data do not provide evidence against power-law tails in the velocity PDF; instead the observed Gaussian PDF is likely a consequence of the comparatively large time scale of observation in the experiment. The second-order, transverse structure functions of normal fluid flow are calculated for the first time ever and conclusively show that the energy spectrum of normal fluid turbulence is decidedly non-classical. The calculated energy spectrum power law, $E(k) \propto k^{-2}$, is shown to be independent of heat flux up to the limitations of the experiment (350 mW/cm^2, $v_n = 2.25$ cm/s).

These novel contributions to the body of quantum turbulence not only provide important guidance for future experimentation, but also provide critical new information, such as boundary conditions and velocity profiles, for the developing theory of quantum turbulence and its numerical simulations. These experiments set the stage for the creation of self-consistent simulations of thermal counterflow and also suggest some obvious avenues of further experimental work. Subsequent experiments must be performed across a broad range of temperatures in helium II and they must probe both steady state counterflow and decaying counterflow, as well as the vortex line density. Such work would benefit from improved sensitivity in 2^{nd} sound attenuation measurements at low heat fluxes, perhaps by using a technique pioneered by Vinen [11] for measuring the characteristic time of vortex line buildup in thermal counterflow. Additionally, there are two natural extensions of the current LIF work being performed on superfluid helium. The first is the investigation and characterization of the normal fluid profile in turbulence generated by a towed grid. Some 2^{nd} sound attenuation experiments for grid turbulence in helium II have

already been performed, initially by Stalp et al. [65]. More recently, these experiments have been extended to a wider variety of grid transparencies [66] and current experiments are characterizing the nature of the superfluid turbulence in much larger channels as a function of grid speed and grid transparency [67]. These experiments lack only important information about the normal fluid flow, which the LIF visualization technique is uniquely suited to provide. Secondly, at temperatures well below 1 K, it is expected that the helium excimers can become trapped by vortex lines. Thus at low temperatures, the LIF technique can be used to visualize the behavior of the vortex lines themselves. A great deal of important groundwork on the trapping diameter has already been done, and shown that not only is the trapping diameter nearly 100 times the radius of an excimer, but also that excimers can be carried through the superfluid by the vortices [68].

That a thin line of excimers can be created in helium gas (§ 2.2.1) presents a number of interesting possibilities for classical turbulence investigation at high Reynolds and Rayleigh numbers (denoted as Re and Ra, respectively). Compared to more common test fluids, such as SF_6 and compressed air, the viscosity (and therefore Re) of cryogenic helium is both easily tunable [69] and spans several orders of magnitude. Cryogenic helium has been used in compact ($L \sim 1$ cm), high Reynolds number ($\sim 10^7$) [70] flow experiments which stand in stark contrast to traditional high Re experiments that require enormous, and enormously expensive, specialized facilities [71]. Indeed, since the LIF technique for flow visualization in helium is applicable in all phases of the fluid, including gaseous helium at its critical point, it is particularly suited to the study of large circulations and structures which are characterized by high Rayleigh and Reynolds numbers [72], but were made infeasible due to the lack of effective visualization and velocimetry techniques in cryogenic helium.

In summary, we have presented the details of an experimental apparatus that can generate a thin line of excimers in superfluid helium and subsequently capture high quality, single-shot images of the molecular line distortion in the counterflowing superfluid.

Image analysis of counterflow at 1.830 K reveals novel structure in the transition of the normal fluid from laminar to turbulent flow. We produce the first ever characterization of normal fluid turbulence and find that the energy spectrum has a decidedly non-classical power law of $E(k) \propto k^{-2}$ across all probed heat fluxes. These experiments (and their extension across a wider temperature range and into decaying counterflow) provide an important contribution not only to our understanding of quantum turbulence, but also are poised to become a valuable new technique in the study of classical high Reynolds and Rayleigh number flows.

APPENDIX: VELOCITY PDFS

The velocity PDFs presented in the main body in the text are reproduced here, but larger and supplemented with PDF plots calculated at intermediate heat fluxes to reinforce the assertion that the velocity PDFs are Gaussian across all probed heat fluxes. For each plot, the red line indicates a Gaussian fit and the heat flux is indicated in the upper left-hand corner.

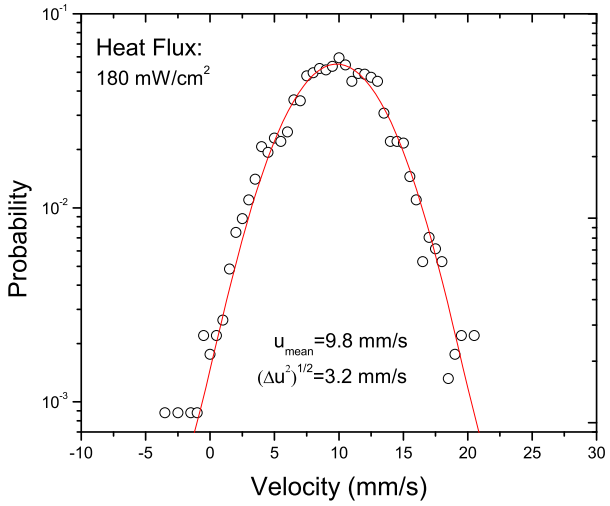

Figure A-1: The normal fluid probability density function for a heat flux of 180mW/cm^2 ($v_n = 1.16$ cm/s).

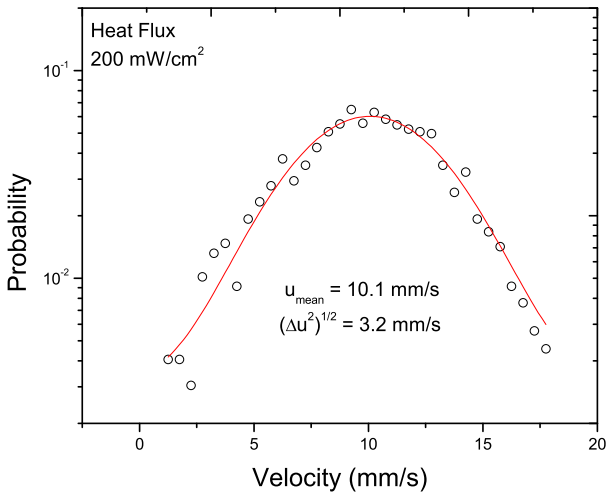

Figure A-2: The normal fluid probability density function for a heat flux of 200mW/cm^2 ($v_n = 1.29$ cm/s).

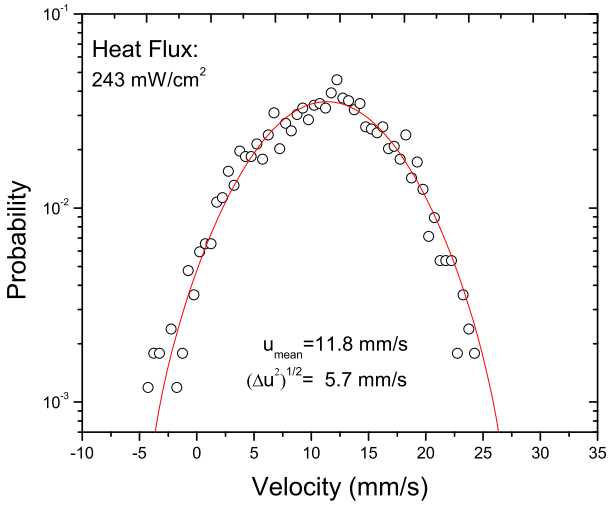

Figure A-3: The normal fluid probability density function for a heat flux of 243mW/cm^2 ($v_n = 1.57$ cm/s).

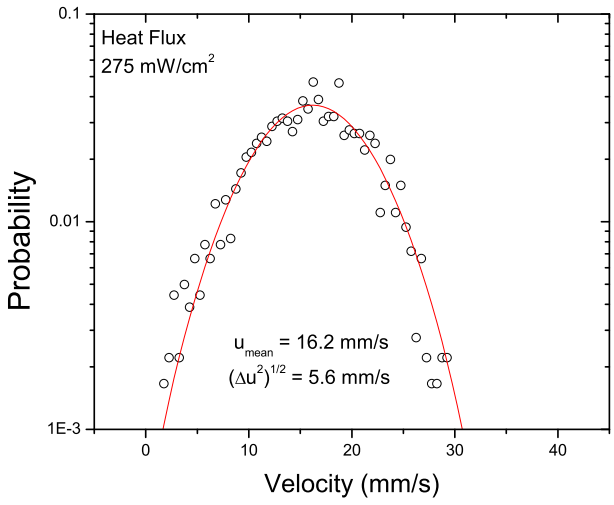

Figure A-4: The normal fluid probability density function for a heat flux of 275mW/cm^2 ($v_n = 1.77$ cm/s).

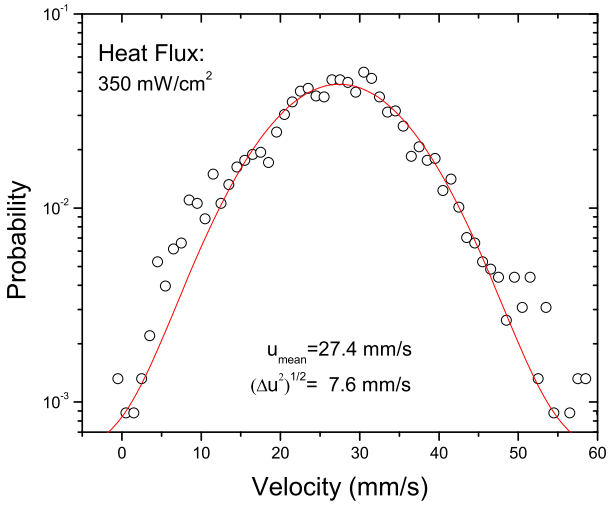

Figure A-5: The normal fluid probability density function for a heat flux of 350mW/cm^2 ($v_n = 2.25$ cm/s).

REFERENCES

[1] H. K. Onnes, Koninklijke Nederlandse Akademie van Wetenschappen Proceedings Series B Physical Sciences **11** (1908).

[2] P. Kapitza, Nature **141** (1938).

[3] J. F. Allen and A. D. Misener, Nature **141** (1938).

[4] L. Tisza, J. Phys. Radium **1** (1940).

[5] L. D. Landau, J. Phys. **5**, 91 (1941).

[6] K. R. Atkins, *Liquid Helium*, edited by N. Feather and D. Shoenberg (Cambridge University Press, 1959).

[7] E. L. Andronikashvili, J. Phys. **10** (1946).

[8] D. S. Greywall and G. Ahlers, Phys. Rev. Lett. **28**, 1251 (1972).

[9] R. J. Donnelly, (2015).

[10] R. P. Feynman, in *Progress in Low Temperature Physics* (North-Holland Publishing Company, 1957).

[11] W. F. Vinen, Proc. R. Soc. Lond. A **243**, 400 (1958).

[12] D. R. Ladner, R. K. Childers, and J. T. Tough, Phys. Rev. B **13**, 2918 (1976).

[13] D. R. Ladner and J. T. Tough, Phys. Rev. B **17**, 1455 (1978).

[14] K. P. Martin and J. T. Tough, Phys. Rev. B **27**, 2788 (1983).

[15] W. F. Vinen, Proc. R. Soc. Lond. A **240**, 114 (1957).

[16] W. F. Vinen, Proc. R. Soc. Lond. A **240**, 128 (1957).

[17] W. F. Vinen, Proc. R. Soc. Lond. A **242**, 493 (1957).

[18] C. J. Gorter and J. H. Mellink, Physica **15**, 285 (1949).

[19] C. F. Barenghi and L. Skrbek, J. Low Temp. Physics **146**, 5 (2007).

[20] R. K. Childers and J. T. Tough, Phys. Rev. B **13**, 1040 (1976).

[21] J. D. Henberger and J. T. Tough, Phys. Rev. B **23**, 413 (1981).

[22] L. Skrbek, A. V. Gordeev, and F. Soukup, Phys. Rev. E **67**, 047302 (2003).

[23] T. Zhang and S. W. V. Sciver, Phys. Fluids (2004).

[24] G. P. Bewley, D. P. Lathrop, and K. R. Sreenivasan, Nature **441**, 588 (2006).

[25] T. V. Chagovets and S. W. V. Sciver, Phys. Fluids **23**, 107102 (2011).

[26] T. Zhang and S. W. V. Sciver, Nature Phys , 36 (2005).

[27] R. E. Packard and T. M. S. Jr, Phys. Rev. A **6**, 799 (1972).

[28] E. J. Yarmchuk, M. J. V. Gordon, and R. E. Packard, Phys. Rev. Lett. **43**, 214 (1979).

[29] M. Paoletti, R. B. Fiorito, K. R. Sreenivasan, and D. P. Lathrop, J. Phys. Soc. Jpn. **77**, 111007 (2008).

[30] D. Kivotides, Phys. Rev. B **77** (2008).

[31] T. Zhang and S. W. V. Sciver, J. Low Temp. Physics **138**, 865 (2005).

[32] D. R. Poole, C. F. Barenghi, Y. A. Sergeev, and W. F. Vinen, Phys. Rev. B **71**, 064514 (2005).

[33] Y. A. Sergeev and C. F. Barenghi, J. Low Temp. Physics **157**, 429 (2009).

[34] M. E. Hayden, G. Archibald, P. D. Barnes, W. T. Buttler, D. J. Clark, M. D. Cooper, M. Espy, R. Golub, G. L. Greene, S. K. Lamoreaux, C. Lei, L. J. Marek, J. C. Peng, and S. I. Penttila, Phys. Rev. Lett. **93**, 103502 (2004).

[35] D. N. McKinsey, C. R. Brome, J. S. Butterworth, S. N. Dzhosyuk, P. R. Huffman, C. E. H. Mattoni, J. M. Doyle, R. Golub, and K. Habicht, Phys. Rev. A **59**, 200 (1999).

[36] A. V. Benderskii, J. Eloranta, R. Zadoyan, and V. A. Apkarian, J. Chem. Phys. **117**, 1201 (2002).

[37] W. G. Rellergert, *Detecting and Imaging He2 molecules in superfluid helium by Laser-Induced Fluorescence*, Ph.D. thesis, Yale University (2008).

[38] W. Guo, J. D. Wright, S. B. Cahn, J. A. Nikkel, and D. N. McKinsey, Phys. Rev. Lett. **102**, 235301 (2009).

[39] W. Guo, S. B. Cahn, J. A. Nikkel, W. F. Vinen, and D. N. McKinsey, Phys. Rev. Lett. **105**, 045301 (2010).

[40] W. Guo, D. N. McKinsey, A. Marakov, K. J. Thompson, G. G. Ihas, and W. F. Vinen, J. Low Temp. Physics **171**, 497 (2012).

[41] A. V. Benderskii, R. Zadoyan, N. Schwenter, and V. A. Apkarian, J. Chem. Phys. **110**, 1542 (1999).

[42] R. S. Berry, Radiation Research **59**, 367 (1974).

[43] J. W. Keto, F. J. Soley, M. Stockton, and W. A. Fitzsimmons, Phys. Rev. A **10**, 872 (1974).

[44] O. Uteza, B. Bussiere, F. Canova, J. P. Chambaret, P. Delaporte, T. Itina, and M. Sentis, Applied Surface Science **254**, 799 (2007).

[45] *Lasers and laser-related equipment – Test methods for laser beam widths, divergence angles and beam propagation ratios – Part 2: General astigmatic beams (ISO 11146-2:2005)* (International Organization for Standardization, 2013).

[46] U. Frisch, *Turbulence* (Cambridge University Press, 1995).

[47] W. H. Miller, J. Chem. Phys. **52**, 3563 (1970).

[48] L. V. Keldysh, Soviet Physics JETP **20**, 1945 (1965).

[49] C. L. M. Ireland and C. G. Morgan, J. Phys. D: Appl. Phys. **6**, 720 (1973).

[50] R. A. Sherlock and D. O. Edwards, Rev. Sci. Instrum. **41**, 1603 (1970).

[51] A. Marakov, J. Gao, W. Guo, S. W. V. Sciver, G. G. Ihas, D. N. McKinsey, and W. F. Vinen, Phys. Rev. B **91**, 094503 (2015).

[52] L. Landau and E. M. Lifshitz, *Fluid Mechanics* (Pergamon Press, Oxford, UK, 1987).

[53] M. Paoletti, M. Fisher, K. R. Sreenivasan, and D. P. Lathrop, Phys. Rev. Lett. **101**, 154501 (2008).

[54] A. Noullez, G. Wallace, W. Lempert, R. B. Miles, and U. Frisch, J. Fluid Mech. **339**, 287 (1996).

[55] W. R. Lempert, P. Ronney, K. Magee, K. R. Gee, and R. P. Haugland, Experiments in Fluids **18**, 249 (1995).

[56] F. Toschi, G. Amati, S. Succi, R. Benzi, and R. Piva, Phys. Rev. Lett. **82**, 5044 (1999).

[57] W. F. Vinen, (Private communication) .

[58] R. G. K. M. Aarts and A. T. A. M. de Waele, Phys. Rev. B **50**, 10069 (1994).

[59] A. W. Baggaley and S. Laizet, Phys. Fluids **25**, 115101 (2013).

[60] S. Yui and M. Tsubota, J. Phys.: Conf. Ser. **568**, 012028 (2014).

[61] A. W. Baggaley and J. Laurie, J. Low Temp. Physics **178**, 35 (2015).

[62] W. Guo, (private communication) .

[63] D. J. Melotte and C. F. Barenghi, Phys. Rev. Lett. **80**, 4181 (1998).

[64] S. Yui and M. Tsubota, "Counterflow quantum turbulence of he ii in a square channel: Numerical analysis with nonuniform flows of the normal fluid," (2015), arXiv:1502.06683v2 [cond-mat.other].

[65] S. R. Stalp, *Decay of Grid Turbulence in Superfluid Helium*, Ph.D. thesis, University of Oregon (1998).

[66] L. Munday, *Quantum Turbulence Generated by Moving Grids*, Ph.D. thesis, Lancaster University (2014).

[67] J. Yang, G. G. Ihas, and W. F. Vinen, Bull. Am. Phys. Soc. **60**, L35.10 (2015).

[68] D. E. Zmeev, F. Papkour, P. M. Walmsley, A. I. Golov, W. Guo, D. N. McKinsey, G. G. Ihas, P. V. E. McClintock, S. N. Fisher, and W. F. Vinen, Phys. Rev. Lett. **110**, 175303 (2013).

[69] D. C. Threlfall, J. Fluid Mech. **67**, 17 (1975).

[70] S. Fuzier, B. Baudouy, and S. W. V. Sciver, Cryogenics **41**, 453 (2001).

[71] M. V. Zargola and A. J. Smits, J. Fluid Mech. **373**, 33 (1998).

[72] R. J. Donnelly and K. R. Sreenivasan, *Flow at Ultra-High Reynolds and Rayleigh Numbers: A Status Report* (Springer, 1998)

BIOGRAPHICAL SKETCH

Alexander Marakov was born in Moscow in 1988. In 1991, his parents made the eminently sensible decision to abandon the USSR in favor of the American Dream. At age 10, Alex made the life-changing decision to become a physicist. In 2010 he received his B.Sc. in Physics from Carnegie Mellon University. He began his graduate studies at the University of Florida Department of Physics in August 2010, receiving a Master's degree in 2013 and, finally graduating with his Ph.D. in 2015.